Acta Materialia 298 (2025) 121423

Contents lists available at ScienceDirect

Acta Materialia

journal homepage: www.elsevier.com/locate/actamat

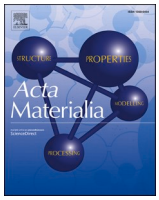

Full length article

Harnessing additive manufacturing-induced microstructure and solute heterogeneities for the design of precipitation-strengthened alloys

Ahmet Turnali [a,*], Avinash Hariharan [b], Efthymios Polatidis [c,d], Nicolas J. Peter [e], Jaqueline Gehlmann [f], Christos Sofras [g], Zoltan Hegedüs [h], Lennart Sayk [i], Tarek Allam [e], Johannes Henrich Schleifenbaum [i], Christian Haase [a,j]

[a] Chair Materials for Additive Manufacturing, TU Berlin, 10587 Berlin, Germany
[b] Steel Institute, RWTH Aachen University, 52072 Aachen, Germany
[c] Laboratory of Technology and Strength of Materials, Department of Mechanical Engineering & Aeronautics, University of Patras, 26500 Patras, Greece
[d] Laboratory for Neutron Scattering and Imaging, Paul Scherrer Institute, PSI, Villigen CH-5232, Switzerland
[e] Institute of Energy Materials and Devices (IMD-1), Forschungszentrum Jülich GmbH, 52428 Jülich, Germany
[f] Central Facility for Electron Microscopy, RWTH Aachen University, 52074 Aachen, Germany
[g] Laboratory for Advanced Materials Processing, Empa, 8600 Dübendorf, Switzerland
[h] Deutsches Elektronen-Synchrotron (DESY), 22607 Hamburg, Germany
[i] Digital Additive Production, RWTH Aachen University, 52074 Aachen, Germany
[j] Center for 3D Technologies, TU Berlin, 10623 Berlin, Germany

ARTICLE INFO

Keywords:
Additive manufacturing
Cellular structures
Dislocation cells
Microsegregation
Multi-principal element alloy
High entropy alloys
Precipitation

ABSTRACT

Solute enrichment at lattice defects is a well-established phenomenon for promoting phase transformations. Metal additive manufacturing (AM) inherently enables this by promoting cellular structures during solidification and thermal cycling. Cellular structures exhibit compositional and lattice defect density variations between cell cores and boundaries, leading to site-specific phase-transformation (e.g., precipitation) behavior that can be selectively activated by post-AM heat treatments. Despite this potential, cellular structures have largely been treated as byproducts rather than intentionally exploited alloy design features. Guided by these insights, we designed a model $Al_{10.5}Co_{25}Fe_{39.5}Ni_{25}$ multi-principal element alloy to intentionally control composition and thus, precipitation driving forces across cellular structures. The alloy composition was computationally selected to promote segregation of a fast-diffusing, precipitate-forming element into the interdendritic regions during solidification in the laser powder bed fusion (PBF-LB/M) process. This segregation aligned with dislocation walls at cell boundaries, creating a "pre-conditioned" state with enhanced chemical driving force and reduced nucleation barrier for precipitation. This targeted design enabled site-specific nucleation and growth of precipitates at cell boundaries during aging. Comprehensive multiscale characterization complemented by *in situ* synchrotron X-ray diffraction confirmed that cellular structures accelerated precipitation, increased precipitate volume fraction and refined the precipitate size compared to the reference state where cellular structures were removed via solution annealing before aging. As a result, the alloy achieved enhanced yield strength (122.2 % increase), and improved tensile properties compared to the reference state. These findings demonstrate the potential of harnessing cellular structures as functional components to control microstructure evolution in precipitation strengthened AM alloys.

1. Introduction

The unique nature of metal additive manufacturing (AM)-derived microstructures calls for a fresh perspective and encourages innovative approaches to microstructure design [1–3]. AM operates through a layer-by-layer fabrication, during which alloys experience highly localized melting and heat treatment of the domains adjacent to the fusion zone. This does collectively drive various physical mechanisms such as rapid melting-solidification and fast thermal shrinkage-expansion cycles. Such conditions result in the formation of a

* Corresponding author.
E-mail address: turnali@tu-berlin.de (A. Turnali).

https://doi.org/10.1016/j.actamat.2025.121423
Received 2 April 2025; Received in revised form 7 July 2025; Accepted 8 August 2025
Available online 8 August 2025

heterogeneous microstructural landscape [4–13], where cellular structures emerge as one of the most prominent sub-grain features. Cellular structures originate from interaction between microsegregation and generation of dislocations that overlap with segregated solutes [13–15]. Consequently, each cell consists of a dislocation-free interior with a relatively uniform composition (hereafter referred to as *cell core*), whereas the boundaries are enriched with alloying elements and host a high density of dislocations.

Accordingly, cellular structures offer regions with compositional and structural gradients, which can be refined to sub-micron scale depending on the specific AM technology employed [16]. These microstructural features substantially impact the mechanical properties of AM parts, with numerous studies showing notable increase in strength [17–20]. Specifically, the dense dislocation walls at cell boundaries act as mild grain boundaries, effectively restricting dislocation movement, while internal stresses from the chemical misfit between the cell boundaries and cores further enhance the resistance against dislocation motion [21–23]. As the size of the cellular structures decreases, the yield strength increases, analogous to the well-known Hall–Petch effect [9,13,18,19,24]. Cellular structures also present an opportunity to influence the microstructure evolution of AM alloys during post-processing by heat treatments [25–33], which in turn affects the resultant mechanical properties. For instance, dislocations can act as diffusion pathways to accelerate dissolution, thereby resulting in faster homogenization at solution annealing temperatures [28]. Meanwhile, localized departure from the nominal composition caused by elemental segregation can accelerate phase transformation kinetics [26] and strongly influence precipitate size and volume fraction [32]. To date, numerous investigations have been carried out to examine post-AM heat treatment of different alloys [29,32–42]. However, a limited number of studies [26,31,43,44] elucidated the phase evolution and transformation pathways, while only a few of them have focused on cellular structures and explored the potential of architecting them through initiating phase transformations to improve mechanical properties [27,29,34,40,42].

Introducing precipitates into a ductile matrix is a powerful way to endow a superior balance of strength and ductility in advanced alloys. Typically, conventionally processed precipitation strengthened alloys are produced using the combination of mechanical processing and heat treatments. However, these approaches are not directly transferrable to AM alloys, where post mechanical processing to induce microstructural modifications is constrained by the simultaneous creation of material and geometry [2,45]. Therefore, this challenge can be addressed by coupling a suitable AM process with a compatible alloy system to naturally form cellular structures that act as “pre-conditioned” templates for controlled phase transformations. In cellular structures, the difference in composition and defect density between cell cores and boundaries reveal local variations in phase stability, which can significantly influence the microstructure evolution. By applying appropriate post-AM heat treatments to promote solute segregation at these defects, phase transformations can be controlled in a site-specific manner and the effects can be tuned to obtain improved material performance [46,47]. The influence of cellular structures can be further enhanced by segregating fast-diffusing, precipitate-forming elements in the interdendritic regions during solidification (i.e., areas with a high density of lattice defects), thereby predefining the chemical driving force for precipitation at the cell boundaries.

Despite the growing recognition of their influence, cellular structures in AM alloys have largely been treated as byproducts rather than intentional microstructure design components. In the current study, we addressed this gap by focusing on an AM alloy design strategy that explicitly incorporates cellular structures to control local composition and thus, precipitation driving forces that vary between cell cores and boundaries. This opportunity is assessed by computationally designing a face centered cubic (fcc) multi-principal element alloy (MPEA) in which segregation of a fast-diffusing, precipitate-forming element occurs in the interdendritic regions during the AM process. The alloy was processed using the laser powder bed fusion (PBF-LB/M) technique to promote the formation of cellular structures. Their presence induced local variations in the chemical driving force for precipitation within the alloy matrix, thereby enabling site-specific precipitate nucleation and growth at the cell boundaries during aging treatment. To quantify their role, solution annealing was employed to eliminate cellular structures before aging, providing a clear reference for comparison of microstructure evolution and mechanical properties. Microstructural changes during aging treatments were captured by multi-scale characterization using scanning electron microscopy (SEM), electron backscatter diffraction (EBSD), atom probe tomography (APT), scanning transmission electron microscopy (STEM), hardness testing, tensile testing and *in situ* synchrotron X-ray diffraction (SYXRD) measurements. Our findings shed light on the interplay between AM-induced cellular structures and the resulting microstructure evolution, providing key insights into their intentional use for designing precipitation-strengthened AM alloys.

2. Alloy design

In our previous study [16], we presented an approach to tailor site-specific chemistry and local chemical driving forces for precipitation within the dendritic microstructures by leveraging microsegregation and thermal conditions during solidification. The predictive capability of combined CALPHAD and multiphase-field (MPF) was utilized to guide alloy selection and microstructure evolution [48,49]. To this end, $Al_xCo_{25}Fe_{(50-x)}Ni_{25}$ MPEA was selected using CALPHAD thermodynamic assessments, while MPF simulations and microstructure characterization were employed to elucidate the combined influence of alloy composition and thermal conditions [16]. During screening, the core goal was to enrich the liquid with the highest possible concentration of fast-diffusing, precipitate-forming solute (in this case, Al), while maintaining a single phase, supersaturated fcc matrix suitable for precipitation during subsequent aging (Fig. 1**a**). Here, the main intention was to decouple B2-NiAl formation from solidification, enabling enhanced control of the microstructure evolution via heat treatments. This intention was motivated by multiple aspects. Firstly, controlling precipitation in the solid state is often more viable than during solidification, where rapid cooling rates, locally varying thermal conditions within the melt pool and limited processing windows in AM make it challenging to precisely tune phase transformations. While increasing the Al content can promote B2-NiAl formation and enhance strength and toughness [50,51], exceeding a critical threshold introduces several challenges. B2-NiAl that forms at interdendritic regions and grain boundaries during solidification tends to be coarse and interconnected, which compromises processability and mechanical properties [52,53]. Their presence can limit ductility and hinder subsequent microstructural refinement unless post-processing, such as hot rolling, is employed [54]. Moreover, high Al levels promote primary bcc/B2-NiAl solidification mode, making it difficult to retain a ductile fcc matrix and increases the risk of hot cracking [53]. In contrast, maintaining the Al content just below the critical threshold preserves the ductile and supersaturated fcc matrix, allowing for selective activation of Al-enriched domains as precursors for B2-NiAl formation through adequate heat treatments. This essentially allows for better control over precipitate volume fraction, size, morphology, crystal structure and mechanical properties.

The alloy composition determined to comply with this rationale was at x = 10.5 at. % Al ($Al_{10.5}Co_{25}Fe_{39.5}Ni_{25}$). Any increase beyond this composition (e.g., x = 11 at. %) led to interdendritic B2-NiAl formation, based on Scheil solidification simulations (Fig. 1**a**). The methods used for alloy screening and validation are detailed in [16]. Our experimental results and simulations showed that interdendritic regions in solidification structure were enriched with Al. Furthermore, the size and frequency of these interdendritic regions were controlled by the degree of undercooling in processes such as ingot casting, directed energy deposition (DED-LB/M), and PBF-LB/M. The latter two processes are well-known to promote the formation of dislocation cells, with

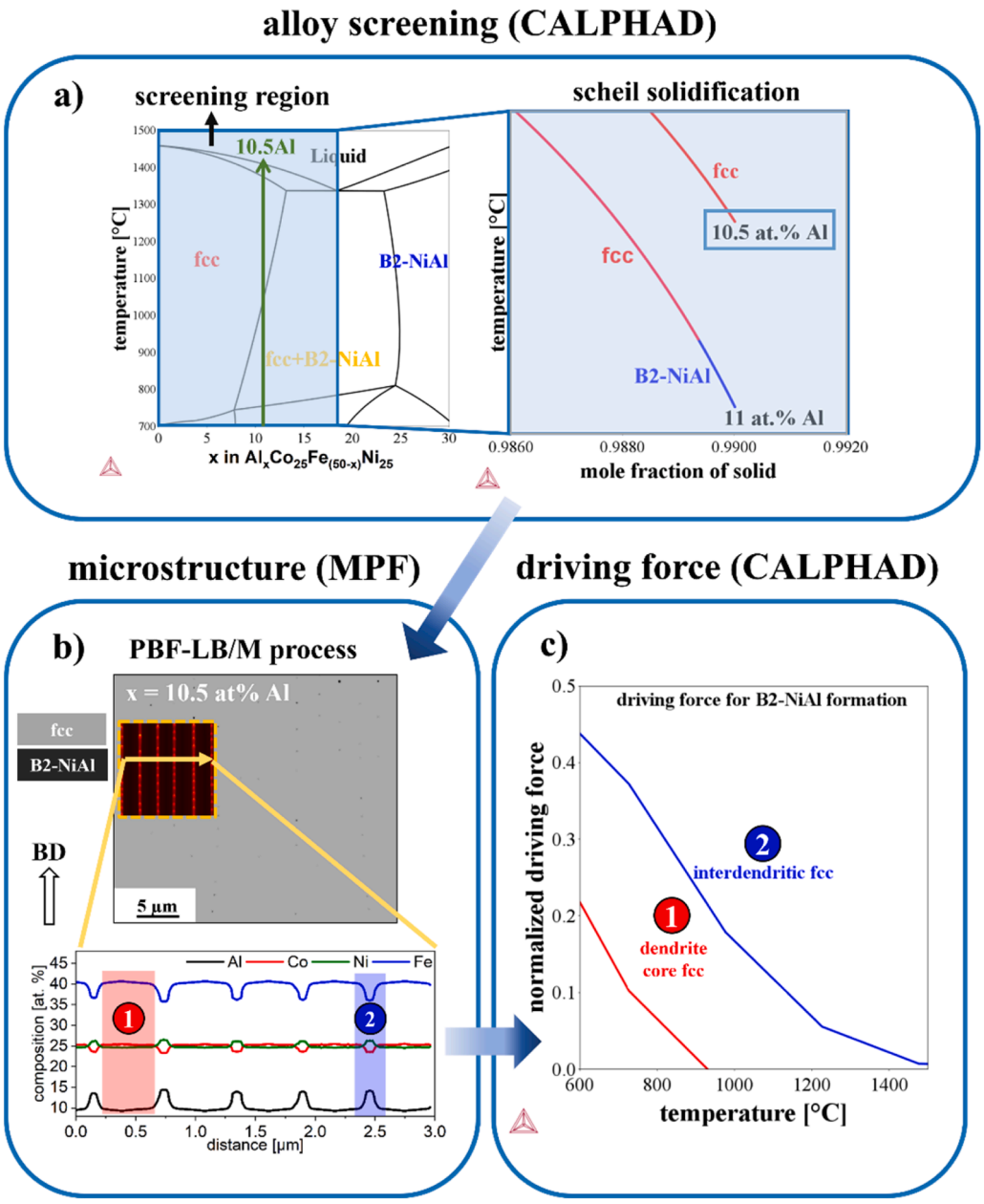

Fig. 1. (a) Equilibrium phase diagram of the $Al_xCo_{25}Fe_{(50-x)}Ni_{25}$ MPEA and Scheil solidification simulations calculated using Thermo-Calc® [56] in combination with a custom thermodynamic database developed for MPEAs [57]. The blue region in phase diagram illustrates the screening region for Scheil solidification simulations and the green arrow shows selected composition at x = 10.5 at. % Al. (b) Multiphase-field simulation (MPF) results for $Al_{10.5}Co_{25}Fe_{39.5}Ni_{25}$ MPEA under PBF-LB/M thermal conditions. The simulation results display the phase map of the as-solidified microstructure. The close-up shows the microsegregation profiles obtained by virtual EDS line-scans. Area 1 in the EDS concentration profile shows the composition in intradendritic regions, while 2 represents the interdendritic composition. (c) Normalized driving force calculations for the $Al_{10.5}Co_{25}Fe_{39.5}Ni_{25}$ MPEA as a function of temperature and local elemental concentration. Calculations were performed by inserting dendrite core and interdendritic elemental concentrations obtained from MPF simulations and demonstrate the possibility for site-specific phase transformation.

PBF-LB/M yielding the smallest cell sizes, due to lower energy density input [9,13,55]. Additionally, dislocation walls in PBF-LB/M are known to overlap directly with primary dendrites [14]. Hence, the PBF-LB/M state of $Al_{10.5}Co_{25}Fe_{39.5}Ni_{25}$ MPEA was selected.

Fig. 1**b** illustrates our computational method to deliberately achieve Al enrichment, along with observed Ni segregation, in the interdendritic regions. This approach aims at enhancing the chemical driving force for precipitation of B2-NiAl phase in these confined areas, as depicted in Fig. 1**c**. Additionally, we seek to align dendrite microsegregation with dislocation cells resulting from the PBF-LB/M process. The motivation is to reduce nucleation barriers and promote solute interactions within these domains through adequate heat treatments to trigger precipitation. In this context, we considered the alloy matrix as "pre-conditioned" in terms of chemical driving forces and nucleation barriers for precipitation, hence, ready to be exploited owing to variations in phase stabilities. The present study builds up on this concept and investigates the quantitative influence of cellular structures on the phase transformations and the resulting effect on the mechanical properties.

3. Materials and methods

3.1. Material and processing

Gas-atomized $Al_{10.5}Co_{25}Fe_{39.5}Ni_{25}$ powders were used for AM employing the PBF-LB/M technique. The chemical composition of both the powder and as-built bulk sample was determined using inductively coupled plasma optical emission spectrometry (ICP-OES) and is summarized in Table 1. Bulk samples for microstructural characterization and mechanical testing were produced using an Aconity-Mini PBF-LB/M machine (Aconity-3D GmbH, Herzogenrath, Germany) equipped with a Yb:YAG fiber laser (400W) with a Gaussian laser intensity profile and a focus diameter of 80 μm. The details regarding powder characterization and printing parameters of $Al_{10.5}Co_{25}Fe_{39.5}Ni_{25}$ alloy can be found elsewhere [16]. The chosen PBF-LB/M parameters facilitated the fabrication of dense bulk samples with a relative density of ≥99.94%, as confirmed by optical residual porosity measurements conducted on as-built cubic samples (**Fig. S1**). Micrographs for porosity analysis were captured using a Keyence VHX-600 digital microscope (Keyence GmbH, Germany), with post-image processing performed using ImageJ® software [58].

Two post-PBF-LB/M heat treatments were designed to establish different initial conditions to induce B2-precipitates, as schematically represented in Fig. 2. The equilibrium phase fractions (X_{eq}) of $Al_{10.5}Co_{25}Fe_{39.5}Ni_{25}$ MPEA as a function of temperature were computed using Thermo-Calc® software [56] 2021b release (Thermo-Calc Software, Sweden) in combination with a custom-constructed multi--principal element alloy database [57]. The equilibrium phase fractions at the heat treatment temperatures is provided in Table 2. In the solution annealing and aging (SA) heat treatment, samples were solution annealed at 1250°C in the single-phase fcc region for 6 h (Fig. 2**a**) and water quenched. Subsequently, the samples were aged at 700°C in the fcc+B2-CoFe+B2-NiAl phase-field, followed by water quenching. The aim of the solution annealing step in SA heat treatment was to provide a modified, less heterogeneous initial microstructure by annihilating cellular structures prior to the aging step at 700°C. In the one-step direct aging (DA) heat treatment, however, the cellular structures remained prevalent, and only one aging step at 700°C was used to induce formation of the B2-CoFe and B2-NiAl phases. These specimens were also water quenched to room temperature after aging.

3.2. Microstructure and mechanical characterization techniques

Microstructure analyses were performed on cubic samples manufactured by PBF-LB/M with dimensions of $5 \times 5 \times 10$ mm^3. The samples were prepared by mechanical grinding up to 2500 SiC grid paper and mechanical polishing with 3 and 1 μm diamond suspension. For scanning electron microscopy (SEM) imaging and electron backscatter diffraction (EBSD) measurements, mechanically polished samples were electropolished at 22 V for 10 s at room temperature using a LectroPol-5 electrolytic polishing machine (Struers GmbH, Germany) and an A2 electrolyte (Struers GmbH, Germany). SEM imaging and EBSD measurements were carried out on a Zeiss Sigma field emission gun (FEG) SEM with EBSD detector (Oxford Instruments plc, Great Britain). SEM micrographs were acquired using backscattered electron (BSE) and inlens detectors at an accelerating voltage of 10 kV, with a working distance between 6 and 8 mm and an aperture size of 75 μm. EBSD measurements were conducted with an accelerating voltage of 20 kV, a working distance between 14 and 16 mm and a step size of 600 nm on a cubic grid. Post-processing of the EBSD data was performed using the MATLAB-based (Mathworks Inc., USA) toolbox MTEX [59–61].

A near atomic scale analysis of the precipitates was performed using atom probe tomography (APT). Needle-shaped specimens were prepared by focused ion beam (FEI Helios Nanolab 660 dual-beam microscope) according to a standard protocol [62,63]. Field evaporation was assisted by laser pulsing using a local electrode atom probe (CAMECA LEAP 4000X HR). Laser pulse frequency, base temperature and detection rate were set at 200 kHz, 60 K and 5 ions out of 1000 applied laser pulses, respectively. The data was post-processed with APT Suite IVAS 6.3 software. The one-dimensional (1D) composition analysis of precipitate chemistry was performed using a cylindrical region of interest (ROI).

Samples for STEM were prepared by conventional metallographic procedures for the as-built material. Three millimeter discs were prepared and ground to a thickness of about 100 μm. Subsequently, the thin discs were dimpled and twin-jet electropolished (Tenupol 5, Struers GmbH, Germany) from both sides until hole formation in the center of the disc. The used electrolyte follows Struers' A2 electrolyte consisting of 6 % perchloric acid, 63 % ethanol and 31 % butylglycol. Conventional sample preparation was used to prevent defect introduction by e.g. focused ion beam preparation to ensure clear lattice defect (dislocation) contrast. In contrast, for the solution annealed material (recrystallized and non-recrystallized grains), local and site-specific sample preparation was necessary. For this purpose, we chose a focused ion beam (Helios 5 PFIB, Thermo Fischer Scientific) lift-out procedure. Final polishing was performed at 5 kV to reduce the amount of surface defects from the sample preparation procedure.

STEM investigations were performed using a probe-corrected Titan G2 80-200 CREWLEY and a probe-corrected Titan Spectra 300 microscope (Thermo Fischer Scientific), which both were equipped with a high-brightness electron gun and a Super-X energy dispersive X-ray spectroscopy (EDS) system. The CREWLEY microscope operated at 200 kV acceleration voltage and with a semi-convergence angle of 24.7 mrad. STEM micrographs were acquired under different imaging conditions to visualize different microstructural features. In particular, high-angle annular dark-field (HAADF) and low-angle annular dark-field (LAADF) images were obtained using collection angles of 69-200 mrad and 37-200 mrad, respectively. HAADF imaging is known to mainly capture mass-thickness contrast variations, which was used to visualize the Ni- and Al-enriched cell boundaries. In contrast, LAADF imaging revealed contrast of strain features in the samples, which was used to visualize dislocations in the sample. It should be noted that the LAADF collection angle range is typically around 10-50 mrad, however, here we refer to a range of 37-200 mrad also as LAADF as strain/diffraction contrast is the dominant contrast mechanism at play in the presented micrographs and not the mass/thickness contrast of HAADF conditions above 70 mrad. The combination of HAADF and LAADF images was used to spatially correlate the predominant dislocation accumulation at the Ni- and Al-rich cell boundaries. The Spectra microscope operated at an acceleration voltage of 300 kV and with a semi-convergence angle of 25.2 mrad. HAADF micrographs in this microscope were acquired at an angular range of 100-200 mrad, while bright-field (BF) images were acquired at an angular range of 0-23 mrad. EDS measurements were in both microscopes employed at a beam current of about 150 pA to visualize the elemental distribution in the sample. Please note that STEM and EDS results acquired in the CREWLEY microscope are presented in Fig. 4, while the results presented in Fig. 7 originate from the Spectra microscope.

Synchrotron X-ray diffraction (SYXRD) measurements were carried out at the beamline P21.2 at PETRA III (DESY, Hamburg, Germany). The as-built and solution-annealed specimens were mechanically ground down to ~1 mm in thickness prior to the measurements. The *in situ* heat treatments were carried out at 700°C using a Linkam TS1500 stage (Linkam Scientific Instruments Ltd., UK). The beamline was operated at

Table 1
Chemical composition (at. %) of the $Al_{10.5}Co_{25}Fe_{39.5}Ni_{25}$ powder and as-built bulk sample measured by ICP-OES analysis.

Elements [at. %]	Al	Co	Fe	Ni
powder	10.8	24.7	39.1	25.4
bulk	10.6	24.5	40.0	24.9

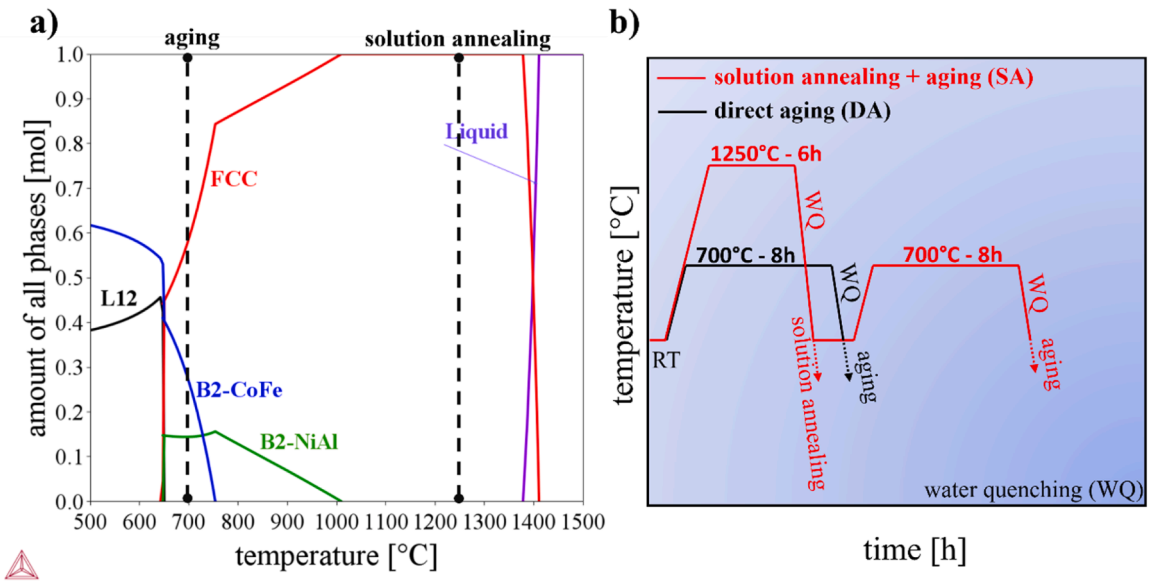

Fig. 2. (a) Equilibrium phase fractions as a function of temperature and (b) post-PBF-LB/M heat treatment regimens of the $Al_{10.5}Co_{25}Fe_{39.5}Ni_{25}$ MPEA.

Table 2
Equilibrium phase fractions (X_{eq}) of $Al_{10.5}Co_{25}Fe_{39.5}Ni_{25}$ MPEA at 1250°C and 700°C.

Phase	fcc	B2-NiAl	B2-CoFe	$L1_2$
X_{eq} at 1250°C [%]	100	0	0	0
X_{eq} at 700°C [%]	58.8	14.4	26.8	0

a fixed photon energy of 82.5 kV yielding an X-ray wavelength of ~ 0.1503 Å. The beam spot size was 150 μm x 150 μm and Varex XRD 4343CT detectors were employed to obtain diffraction patterns. The *in situ* SYXRD dataset was processed to generate 1D diffractograms from 2D diffraction rings via the GSAS II [64] software. Subsequently, sequential peak fitting was applied to investigate changes in lattice parameters and peak intensities, while Rietveld refinement was conducted to determine the changes in phase fractions. Rietveld refinement was undertaken with GSAS-II by integrating the diffraction image of one of the Varex panels along the entire azimuthal range. Starting from the last histogram (i.e. for the longer isothermal time), and after refining the lattice parameters of the γ-fcc and B2-bcc phases, the phase fractions were refined. Then, a cylindrical symmetry texture model using a 12 and 8 harmonic order for the γ-fcc and precipitates was used to model the crystallographic texture. An isotropic microstrain model was used for modeling the peak broadening in all phases. The background was fitted using a Chebyshev polynomial of 8 orders. The backward sequential refinement (towards shorter annealing time) of all data was undertaken by refining the phase fractions, the microstrain model, the texture and hydrostatic/elastic strain to capture the lattice strain evolution in all phases. The maximum number of refinement cycles was set to 10 and the refined parameters were propagating to the next histogram.

To assess tensile properties, vertical cylindrical samples were manufactured parallel to the building direction. Cylindrical samples for both as-built and heat treated conditions were machined into B4 × 20 tensile specimens according to DIN 50125. Quasi-static uniaxial tensile tests were conducted at room temperature on a Z100 mechanical testing device (Zwick/Roell GmbH & Co. KG, Germany) with a constant strain rate of 0.00025 s^{-1} until fracture. Each condition underwent testing on a minimum of three specimens, and the results shown represent the average values obtained.

4. Results

4.1. Microstructures of the initial states

Fig. 3 shows the microstructure of the as-built and solution annealed states. Inverse pole figure (IPF) maps of the as-built state revealed that large columnar grains were epitaxially grown over several melt pools, resulting in an elongated grain morphology along the building direction (BD). These elongated grains often exhibited gradients in local orientation distribution within individual grains, as indicated in the IPF orientation map. The IPF orientation map and grain boundary map in Fig. 3 displayed that the local misorientations coincided with the low-angle grain boundaries (LAGBs) ($2^\circ < \Theta < 10^\circ$), constituting 41.4% of all grain boundaries in the microstructure. The as-built microstructure also demonstrated large grain orientation spread (GOS) values, indicating high intragranular misorientations. Moreover, the obtained GOS values were higher in the deformed grains as compared to the recrystallized (RX) grains with reduced dislocation densities [65]. Correspondingly, the as-built state was characterized by almost an order of magnitude larger estimated geometrically necessary dislocation (GND) density (1.1×10^{14} m^{-2}), compared to the solution annealed state (3×10^{13} m^{-2}). The criterion of GOS < 2° was used to determine the RX area fraction of the microstructure after solution annealing. The RX area fraction in solution annealed state accounted for 66.5%, and a transition from elongated grain morphology to mixed columnar/equiaxed grain morphologies was observed. Moreover, EBSD analysis showed that the majority of the annealing twins were aggregated in RX grains, whose formation were induced by high initial dislocation densities inherited from the as-built state [39]. Despite the substantial portion of RX grains, non-recrystallized (non-RX) grains with high GOS values remained after solution annealing, encompassing most of the LAGBs (with the fraction reduced to 10.4%) and exhibiting higher GND densities compared to the RX grains.

Fig. 4 shows the SYXRD diffractograms and STEM images of the as-built and solution annealed states extracted from cross-sections parallel to the building BD. According to SYXRD measurements, both initial states were comprised of a single-phase solid solution fcc crystal structure (Fig. 4**a**). From Fig. 4**b**, the as-built state exhibited cellular structures (dislocation cell diameter $d_c = 578 \pm 53$ nm) in columnar grains. The dislocations at cell boundaries coincided with Al and Ni microsegregation at interdendritic regions, confirming the computational predictions (Fig. 1**a** and **b**). The darker spherical features observed in

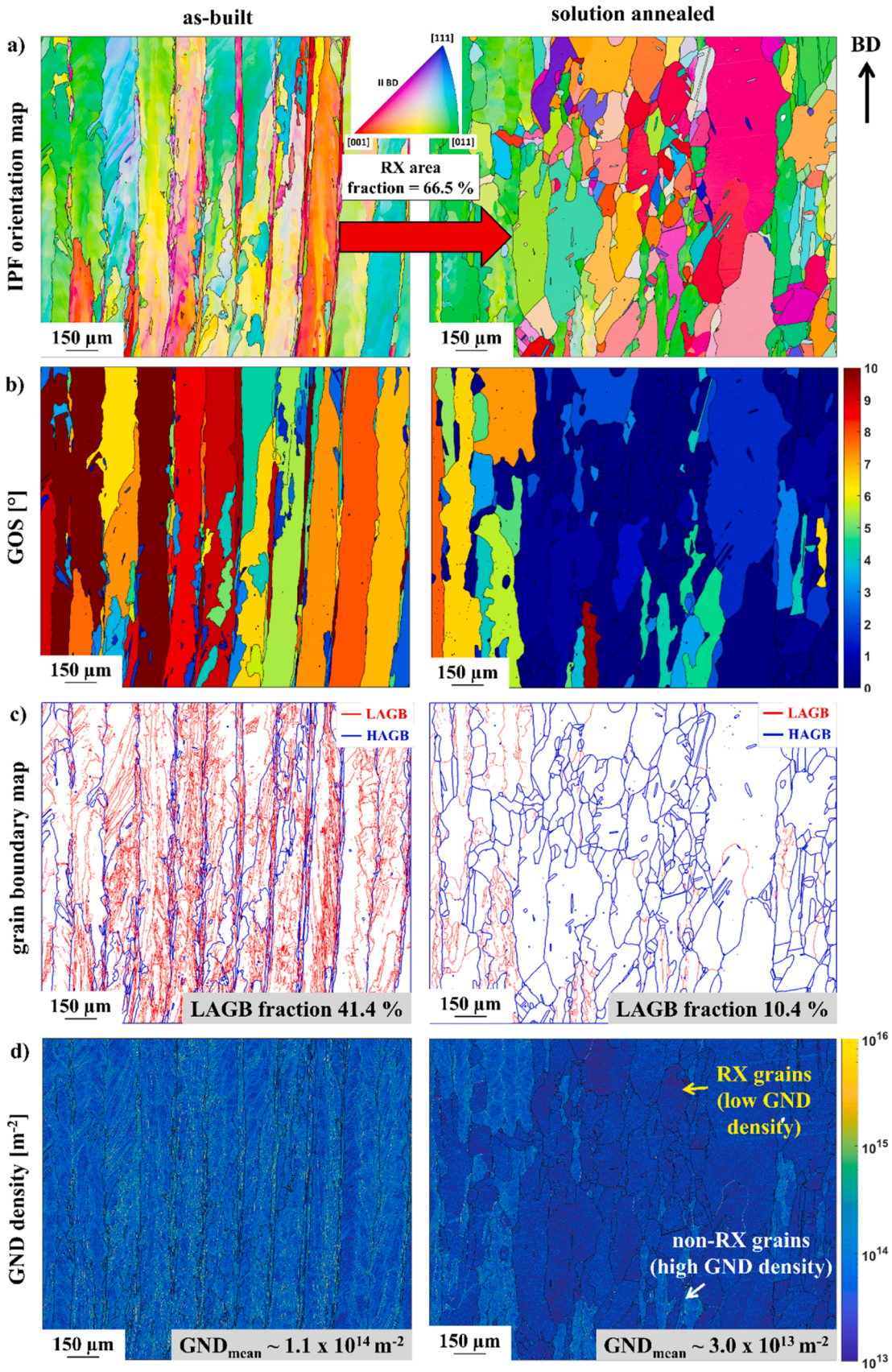

Fig. 3. EBSD analysis of the as-built and solution annealed states. EBSD measurements were acquired from the center of the cross-section parallel to build direction (BD). (a) EBSD inverse pole figure (IPF) orientation maps with BD as reference axis, (b) grain orientation spread (GOS) maps, (c) grain-boundary maps, and (d) geometrically necessary dislocation (GND) density maps. Blue and red lines in (c) denote high-angle (misorientation angle $\Theta > 10$ °) and low-angle ($2° < \Theta < 10°$) grain boundaries, respectively.

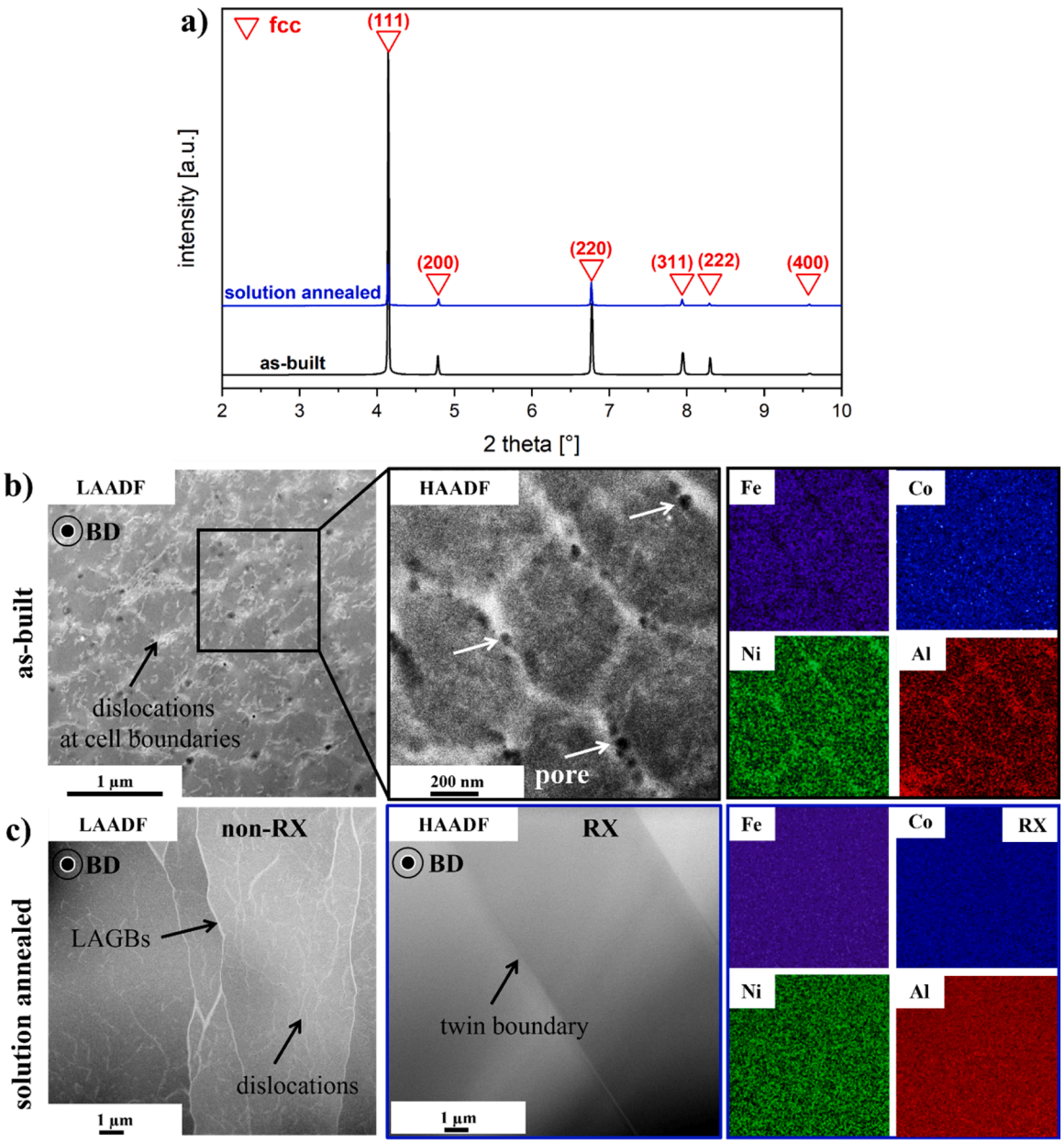

Fig. 4. Characterization of the initial states via SYXRD, STEM and SEM. The examined cross section corresponds to the plane perpendicular to the building direction (BD). (a) Integrated 1D diffractograms from SYXRD 2D patterns. (b) STEM strain contrast images showing high dislocation densities arranged in cellular patterns and STEM HAADF image displaying segregation of Ni and Al on cell boundaries with corresponding Fe, Co, Ni, Al EDS elemental maps. (c) STEM HAADF images of non-RX and RX grains in the solution-annealed sample. EDS elemental maps correspond to the area of RX grains.

Fig. 4**b** are identified as pores, as confirmed by clarification provided in the Supplementary (**Fig. S2**). The solution annealed state exhibited a mixture of non-RX and RX grains (Fig. 4**c**, see also Fig. 3). In contrast to the as-built state, the solution annealed state displayed no cellular structures within these grains, but some of the non-RX grains were able to preserve the LAGBs. Moreover, EDS measurements revealed that the RX grains exhibited homogeneous elemental distribution. This observation confirmed that cellular structures were thermally unstable and vanished during solution annealing at 1250°C after 6h.

4.2. *Microstructure evolution during aging*

Fig. 5 and Fig. 6 display the microstructural evolution during aging, as assessed by post-mortem SEM (in-lens) examination for both the DA and SA states over the aging duration at 700 °C. Prior to aging, neither state showed the presence of a second phase according to the SYXRD measurements (Fig. 4**a**). Representative SEM images of the as-built and solution annealed states are provided in the **Fig. S3**, reaffirming that cellular structures were present in the as-built grains but absent after solution annealing. During the initial 0.5h of aging in the DA treatment, precipitates preferentially formed along Al- and Ni-enriched cell boundaries, while the cell cores remained precipitate-free (Fig. 5**a–c**). Both nanoscale and larger plate-like precipitates were observed, with the larger precipitates emerging near process-induced defects such as pores. With extended holding time (e.g., at 1h), cell boundaries became completely decorated with precipitates (Fig. 6**a-c**) that were growing towards the cell cores, resulting in a heterogeneous number density across the fcc matrix. The precipitates exhibited a plate-like morphology and interacted in a characteristic zig-zag pattern along the prior cell boundaries, as highlighted by white dashed lines in Fig. 6**b**. This

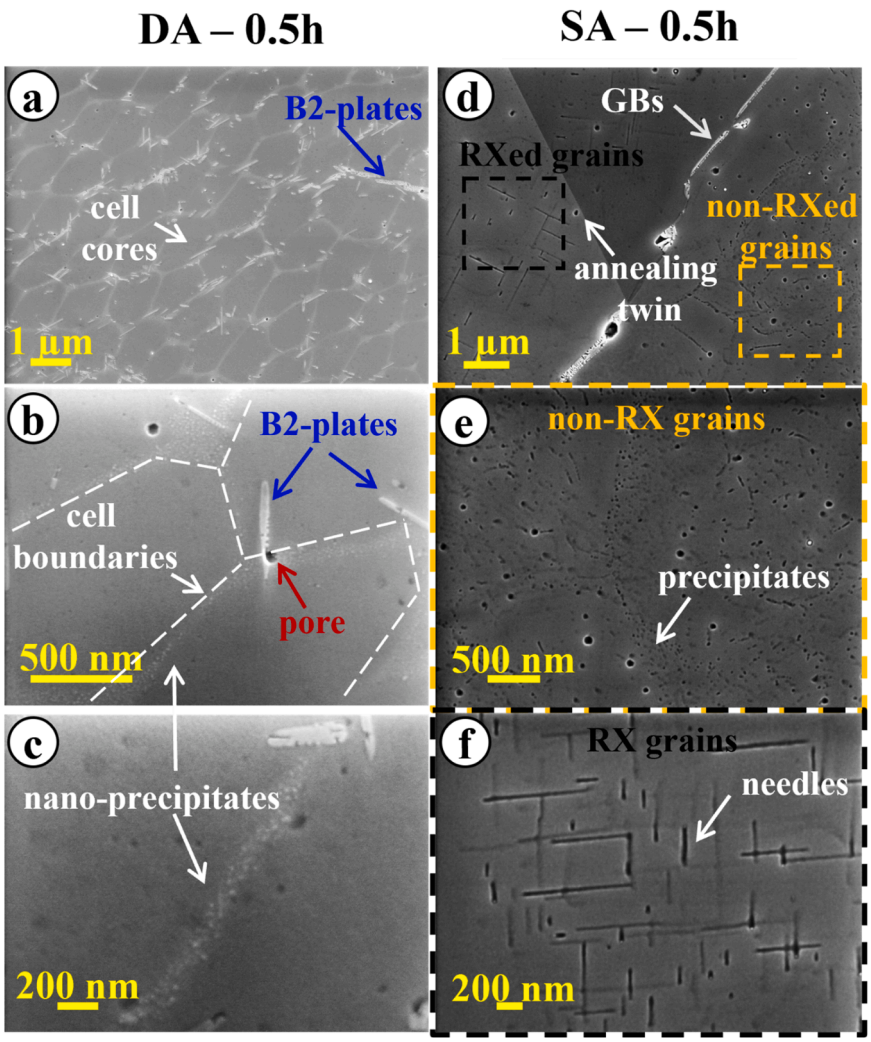

Fig. 5. SEM (in-lens) characterization of microstructural changes in the DA and SA within the first 0.5h of the aging process at 700°C. (a-c) DA – 0.5h state, (d-f) SA – 0.5h state.

alignment of precipitates along former cell boundaries was also observed in other grains (Fig. 6**a**), further emphasized by yellow arrows indicating the growth trajectories of the former cell boundaries originating from the bottom of the melt pools. The images also show that cells with different morphologies coexist across different grains (e.g. cellular or columnar, Fig. 5**a** and Fig. 6**a-b**) since they naturally adopt crystallographic orientations of the underlying grain structure [14,66]. Additionally, co-precipitation was apparent in SEM images, as visually evident from the distinct morphologies of darker and lighter regions within the precipitates, suggesting the presence of multiple phases. At the end of the DA treatment (8h, Fig. 6**d-f**), precipitates continued to grow, interacted by extending towards the cell core, and dispersed throughout the fcc matrix.

In comparison to the DA heat treatment, the SA heat treatment led to a distinctly different precipitation behavior, as evidenced by the morphologically different precipitates appeared in the RX and non-RX grains. To comprehensively monitor this behavior, SEM micrographs were specifically captured from both grains and from various regions across the microstructure (Fig. 5**d-f** and Fig. 6**g-k**). During the first 0.5h, precipitates in RX grains mostly showed needle-shaped morphologies with high aspect ratios and perpendicular alignment to each other. The precipitates in non-RX grains displayed irregularities in their morphology and spatial distribution (Fig. 5**d-f**). After 8h (Fig. 6**g-k**), non-RX grains showed clear signs of co-precipitation, visible as small dark features embedded within larger light-contrast precipitates (Fig. 6**i**), similar to the morphologies observed in the DA condition (Fig. 6**f**). In contrast, RX grains remained mostly free of large precipitates, with occasional precipitate formation observed primarily around process-induced pores (Fig. 6**j-k**). This led to a heterogeneous spatial distribution of large precipitates across the microstructure of solution annealed state.

4.3. *Precipitate analysis*

STEM-EDS analysis was conducted to qualitatively reveal chemical characteristics of the co-precipitation behavior in the DA condition at different aging stages (Fig. 7). In the DA – 0.5h state (Fig. 7**a**), precipitates decorated the former cell boundaries, consistent with the SEM observations in Fig. 5**a–c**. Dislocations were also observed surrounding the growing precipitates and within the cell interiors, revealing their rearrangement during aging. Elemental maps confirmed the sustained Ni and Al enrichment from the as-built state along cell boundaries, accompanied by Co and Fe depletion. The precipitates were similarly enriched in Ni and Al, indicating that the primary precipitates forming in the early stages of aging were predominantly Ni- and Al-based. After 8h of aging (Fig. 7**b**), the precipitates had grown substantially and interacted across the fcc matrix, as also shown previously in Fig. 6**d–f**. In HAADF imaging (Fig. 7**b**), precipitates exhibited both dark and bright contrasts, suggesting compositional heterogeneity within individual precipitates. EDS analysis revealed that Ni- and Al-rich regions

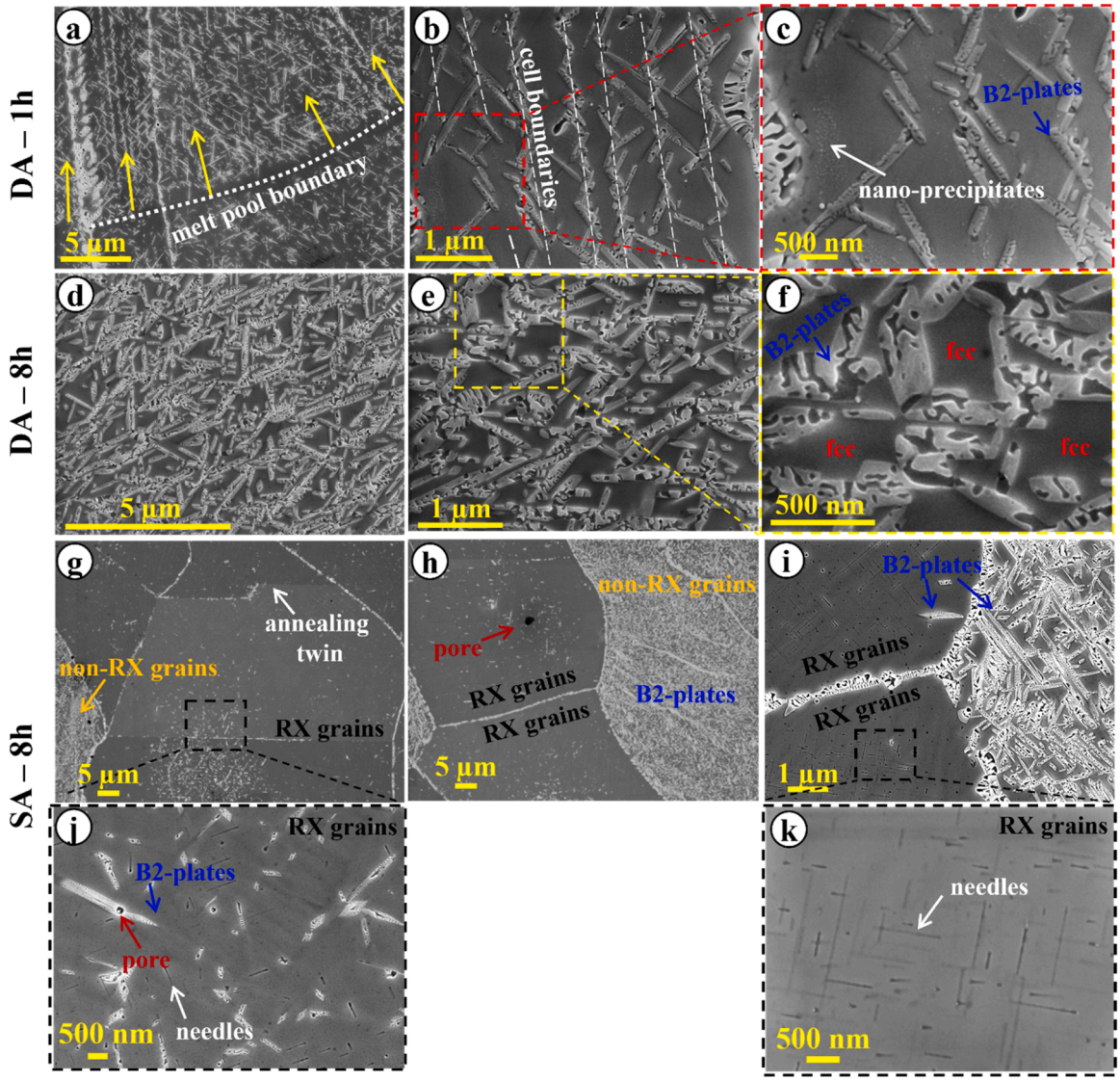

Fig. 6. Microstructure evolution in the DA and SA states captured by SEM (in-lens) at specified time intervals over the duration of the aging process at 700°C. (a-c) DA – 1h state, (d-f) DA – 8h state, (g-k) SA - 8h state.

constituted the matrix of the large precipitates, while Co- and Fe-rich domains were embedded within them, indicating co-precipitation of NiAl- and CoFe-rich phases. Additionally, precipitates enriched in Ni and Al but depleted in Co and Fe were identified, highlighting the dominant role of Ni and Al in driving precipitation (Fig. 1**c**). Similar co-precipitation behavior was observed in the SA – 8h condition as presented in Fig. 6**g-k**. Corresponding STEM-EDS characterization is provided in the **Fig. S4** to support these observations.

To understand the structural characteristics of the precipitates, a detailed analysis was conducted by SYXRD (Fig. 8 and **Fig. S5)**. The *in situ* evolution of raw SYXRD diffraction patterns are shown in **Fig. S5.** Precipitates were initially identified as ordered B2 phase, as indicated by the presence of the superlattice $B2_{(100)}$ reflection in the SYXRD patterns (**Fig. S5**). Analysis of peak positions revealed a high lattice misfit of approximately 20% between the B2-precipitates and the fcc matrix, suggesting no crystallographic coherency [50]. To interpret the observed co-precipitation behavior in both states, *in situ* evolution of higher-order bcc reflections were examined due to their improved resolution for detecting subtle peak splitting (Fig. 8). Notably, the $bcc_{(220)}$ peak exhibited shoulders (Fig. 8**a**), indicative of overlapping reflections from two phases with slightly different lattice parameters. Peak deconvolution was performed using a Voigt function to resolve the individual peak components at the end of the aging (Fig. 8**b**), and the corresponding lattice parameters were calculated using Bragg's law, based on the determined peak positions, interplanar spacing, and the corresponding Miller indices. The left peak yielded a lattice parameter of 2.925 Å, while the right corresponded to 2.919 Å. These values align well with the theoretical lattice parameters of CsCl-prototype (space group $Pm\bar{3}m$, no. 221) B2-NiAl (~2.86 Å) [67] and B2-CoFe (~2.84 Å) [68], with the larger lattice parameter of B2-NiAl resulting in a reflection at a lower 2 theta values according to Bragg's law. The slight deviations from theoretical lattice parameters can be primarily attributed to the non-stoichiometric nature of both B2-precipitates in the current study. Rather than existing as pure binary compounds, both B2-NiAl and B2-CoFe contained all four elements with varying compositions across their respective sublattices as further represented via the equilibrium thermodynamic calculations and APT measurements (Table 3). In particular, B2-NiAl remains enriched in Ni and Al, but incorporates a measurable amount of Co and Fe, and vice versa for B2-CoFe. Additionally, the observed peak asymmetry may also reflect the contributions from localized strains, which can introduce variation in lattice spacings of B2-phases [26,69]. Lastly, although peak splitting was not consistently observed across all reflections, e.g., lower order peaks, qualitative comparisons with STEM-EDS measurements confirm the

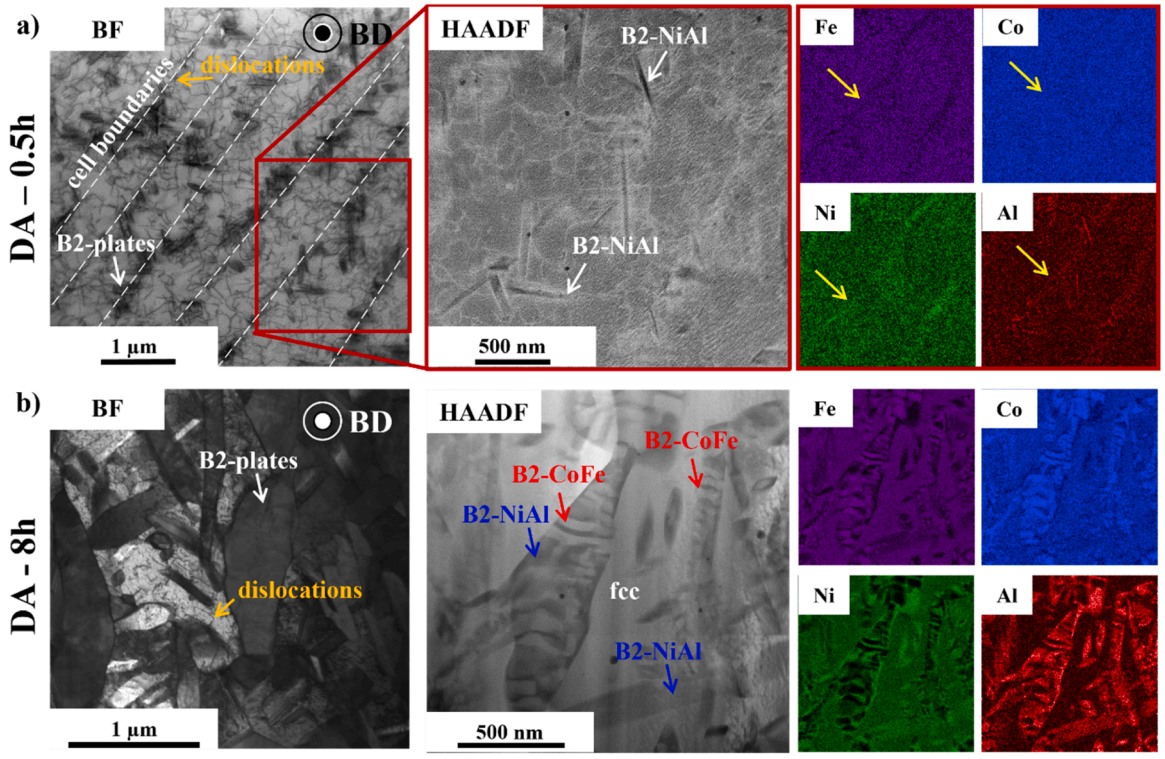

Fig. 7. Characterization of DA states via STEM. The examined cross section corresponds to the plane perpendicular to the BD. (a) DA – 0.5 h state. The STEM bright-field (BF) image reveals high dislocation densities along the former cell boundaries. The corresponding HAADF image shows Ni and Al enrichment (yellow arrows) along these boundaries and the formation of the B2-NiAl phase, with corresponding Fe, Co, Ni, Al EDS elemental maps. (b) DA – 8 h state. The STEM BF image reveals large B2-plates and dislocations in the fcc matrix. The HAADF image demonstrates co-precipitation of B2-NiAl and B2-CoFe phases, as supported by Fe, Co, Ni, and Al EDS maps. Precipitates with darker contrast correspond to B2-NiAl, while those with brighter contrast represent B2-CoFe.

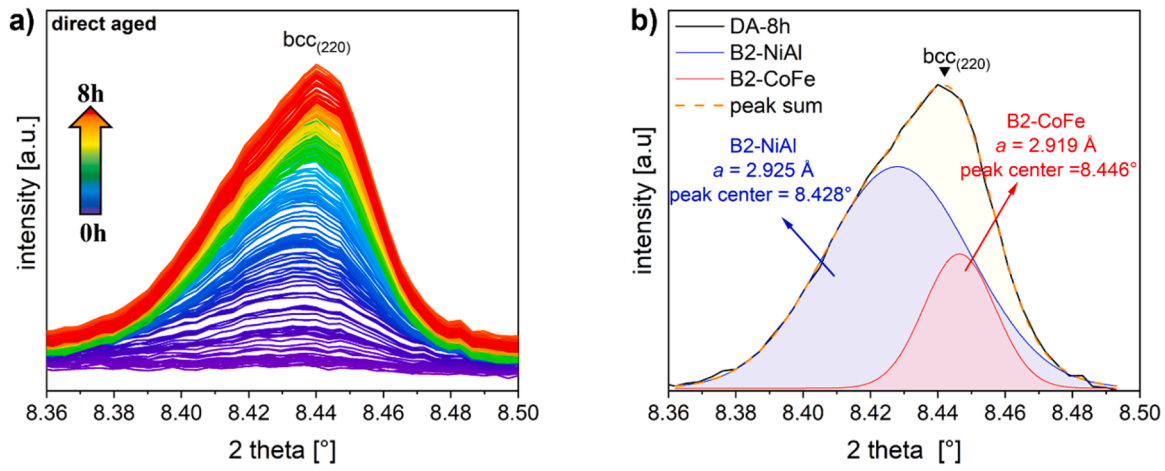

Fig. 8. (a) *In situ* evolution of $bcc_{(220)}$ peaks during direct aging. (b) Demonstration of peak splitting in higher-order $bcc_{(220)}$ reflection, indicating the co-existence of B2-NiAl and B2-CoFe phases at the end of the DA treatment.

co-precipitation of B2-NiAl and B2-CoFe (Fig. 7**b**). Thus, when comparing the information obtained from SEM characterization (Fig. 6**d-f**), STEM-EDS analysis (Fig. 7**b**) and SYXRD measurements (Fig. 8), it was clear that the lighter precipitates with a higher area fraction in SEM (Fig. 6**d-f**) represented the B2-NiAl phase. In contrast, the smaller, darker precipitates within the large B2-NiAl plates were identified as B2-CoFe, which appeared to have a lower area fraction.

The size and morphology of co-precipitated domains were characterized at the end of the 8h aging (Fig. 6) and quantitative measurements were digitally performed using ImageJ®. For this purpose, B2-NiAl and B2-CoFe phases were treated as discrete, uniform domains. In the DA-8h condition, precipitates exhibited an average width of 117.8 ± 41.4 nm and a length of 557.1 ± 282.2 nm. In contrast, larger precipitates were observed in the non-RX grains of the SA-8h condition, with an average width of 144.6 ± 31.9 nm and length of 902.5 ± 351.9 nm. Within RX grains, the precipitates retained a fine, needle-shaped morphology with high aspect ratios, averaging 52.9 ± 16.4 nm in width and 683.3 ± 295.3 nm in length.

To quantify solute partitioning and precipitate chemistry throughout aging, APT was employed. The 3D APT reconstruction and the corresponding 1D-elemental profiles of the heat treated states (DA and SA) are presented in Fig. 9 and 10. Corresponding 1D-elemental profiles

Table 3
Equilibrium phase compositions (p_{eq}) of $Al_{10.5}Co_{25}Fe_{39.5}Ni_{25}$ MPEA at 700°C, as calculated using Thermo-Calc® software, compared with 1D-elemental profiles from ROIs in APT measurements (Figs. 9 and 10).

Phase	Al [at. %]	Co [at. %]	Fe [at. %]	Ni [at. %]
p_{eq} fcc	8.0	21.4	39.7	30.9
p_{eq} B2-NiAl	25.7	15.4	22.7	36.2
p_{eq} B2-CoFe	7.8	38.0	48.2	6.0
DA – 0.5h (B2-NiAl)	30.7	20.6	21.9	26.8
DA – 0.5h (B2-CoFe)	12.6	30.5	47.9	9.0
DA – 0.5h (interface)	19.4	21.6	37.4	21.6
DA – 8h (B2-NiAl)	25.3	19.3	23.6	31.8
DA – 8h (B2-CoFe)	7.8	35.1	50.2	6.9
SA – 8h (1)	52.8	9.0	24.4	13.8
SA – 8h (2)	33.4	13.1	32.9	20.6

were extracted along cylindrical regions of interest (ROI). To understand the localized phase transformation behavior during the DA heat treatment, site-specific APT tips were extracted from the cell boundaries of the DA - 0.5h state (Figs. 9**a-b**). Lift-out locations were provided in **Fig. S6**. In Fig. 9**a**, the first 30 nm of the 1D-elemental profiles correspond to the matrix. The matrix-precipitate interface displayed excess Fe and Al depletion due to solute rejection and partitioning during precipitation that initiated the co-precipitation of B2-NiAl and B2-CoFe precipitates (Fig. 9**a**), whereas their compositions were far from equilibrium (Table 3). Moreover, the near-spherical B2-CoFe precipitate was identified from the 1D-elemental profile. To gain further insights into precipitate nucleation, another tip was extracted from a cell boundary of the DA - 0.5h state (Fig. 9**b**). While approaching the cell boundaries, Al enrichment was identified from the Al spike at 19.4 at. %, as well as depletion of Ni, Co and Fe, compared to the equilibrium matrix composition (p_{eq} fcc, Table 3). These observations aligned with the enrichment of Al inherited from as-built state (Figs. 4 and 7), which acted as a precursor for the nucleation of the B2-NiAl phase on cell boundaries. At the end of the DA heat treatment (8h), co-precipitation of B2-NiAl and B2-CoFe proceeded, forming large B2-plates that were approaching equilibrium concentration (Table 3).

Fig. 10 shows the APT analysis of needle-shaped precipitates observed in RX grains (Fig. 6**k**). Cylindrical ROI represented with 1 was taken from the junction of the precipitate, whereas ROI 2 was taken from the branches of the precipitates. At junction (1), Al enriched up to 53 at. %, whereas it reached a maximum of 33.5 at. % at the branch (2). In both measurement points, the needles were showing an Al-rich, non-equilibrium composition (Table 3).

4.4. Precipitation kinetics and mechanical properties

To place the microstructure evolution during aging into a quantifiable context, the changes in total precipitate volume fraction and corresponding hardness values are presented in Fig. 11**a**. The complete dataset is summarized in Table 4. Complementing this, *in situ* SYXRD was employed to monitor solute depletion from the fcc matrix and the time-dependent formation of precipitates (Fig. 11**b** and **c**). The raw 1D-diffraction patterns are also shown in **Fig. S5,** which also illustrate *in situ* evolution of $fcc_{(111)}$ and $bcc_{(110)}$ main peaks and $B2_{(100)}$ superlattice peak for both DA and SA states.

Prior to aging, the as-built state exhibited a higher hardness (221 ± 3 HV10) compared to the solution annealed condition (173 ± 3 HV10). After 0.5h of DA, the B2 volume fraction increased to 3.8%, accompanied by a drop in the fcc lattice parameter and a sharp rise in the integrated intensity of the $B2_{(100)}$ superlattice reflections (Fig. 11**b** and **c**). These microstructural changes coincided with an increase in hardness to 254 ± 6 HV10 (Fig. 11**a**). With prolonged aging time, peak hardness of 420 ± 8 HV10 was attained at approximately 4h and total B2 volume fraction reached 27.9 % (Fig. 11**a** and Table 4). During this period, the fcc lattice parameter exhibited higher decrease rates, indicative of accelerated chemical change due to solute rejection and partitioning during precipitation (Fig. 11**b**). The decrease in lattice parameter during the DA heat treatment was also reflected by a shift of the $fcc_{(111)}$ peak to higher 2 theta values and a reduction in its intensity, which was accompanied by a monotonic intensity increase of the $B2_{(100)}$ superlattice and $B2_{(110)}$ reflections (**Fig. S5**). During the remainder, the precipitation kinetics slowed down, as reflected by the plateauing of the total B2 volume fraction, a modest reduction in fcc lattice parameter, and a slight decrease in hardness to 411 ± 5 HV10. This suggested that the formation of B2-precipitates was most active during the initial 4h, while it was decelerated towards the end DA heat treatment (8h).

In contrast to the DA heat treatment, the SA heat treatment led to a lower total precipitate volume fraction and hardness values (Fig. 11**a** and Table 4). During the first 4h of SA, the fcc lattice parameter exhibited only a minor reduction, the total B2-volume fraction increased by 5.7%, and the hardness rose moderately. Between 4h and 8h, however, the solute removal from fcc accelerated, as evidenced by a steeper decline in fcc lattice parameter and a more pronounced increase in the $B2_{(100)}$ superlattice intensity (Fig. 11**b** and **c**). Resembling the DA state, such a decrease in fcc lattice parameter was translated as the shift of the $fcc_{(111)}$ peak to higher 2 theta values (**Fig. S5**). This corresponded to an increase in hardness to 305 ± 16 HV10. Yet, such an increase in hardness was not reflected in the increase in total B2-fraction, which only rose by 7.6 % between 4h and 8h of aging, compared to 5.7 % within the initial 4h.

Tensile properties of the initial and aged states are presented in Fig. 12, and the corresponding characteristic tensile properties are listed in **Table S1**. Compared to the solution annealed state, the as-built state exhibited higher yield strength and ultimate tensile strength, but lower uniform elongation and elongation at fracture. The DA heat treatment resulted in a strength and ductility trade-off with a gradual increase in strength and decrease in ductility, as the total B2-fraction continuously increased during the first 4h of aging (Table 3). Consequently, yield strength ($R_{p0.2}$) and ultimate tensile strength (R_m) rose to 951.8 ± 19 and 1237.6 ± 23.4 MPa, respectively, while considerably good elongation (uniform elongation, A_g, of 12.4 ± 0.9% and elongation at fracture, ε_f, of 14.1 ± 1.8%) was maintained despite the large volume fraction (30.1%) of B2-precipitates. This indicates an almost two-fold increase in strength, whereas the ductility decreased by almost 30% as compared to the as-built state.

Strength and ductility trade-off were also observed after the SA heat treatment. Accordingly, $R_{p0.2}$ and R_m increased to 428 ± 3.5 and 703.2 ± 3.5 MPa, respectively, whereas A_g of 32.0 ± 0.8% and ε_f of 41.1 ± 2.0% was attained. However, the increase in strength and reduction in ductility were relatively minor compared to the DA state, regardless of the total B2-fraction of 13.3 %.

5. Discussion

5.1. Heterogeneity-mediated microstructure evolution

The results revealed profound differences in precipitation behavior between the as-built and solution annealed states during aging treatment. The DA state exhibited site-specific initiation of precipitate nucleation and subsequent growth into the alloy matrix from spatially confined regions associated with cell boundaries. The annihilation of cellular structures in the SA state not only resulted in significant reduction in nucleation rate, but also a difference in precipitate volume fraction, size and morphology over the complete aging duration of 8h.

In the current study, the microstructure of the as-built state contains local gradients in elemental concentration and dislocation density. Based on previous studies [14,15], *in situ* heating and cooling cycles throughout the AM processes known to lead to the formation of residual stresses and strains caused by thermal shrinkage and expansion, which have been identified as the primary source for dislocation formation and their rearrangement into cellular patterns. In PBF-LB/M, the natural

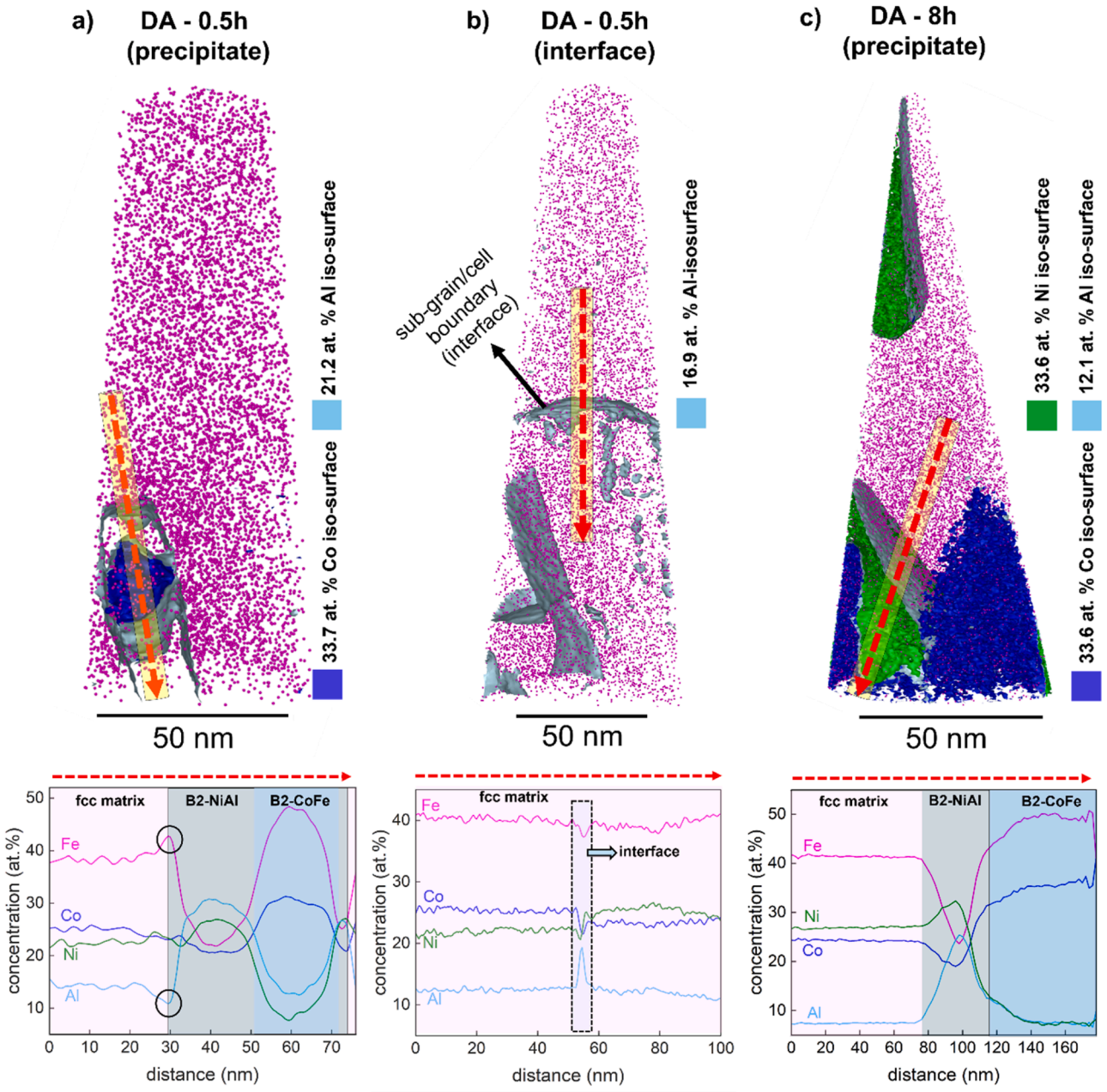

Fig. 9. APT analysis and respective 1D-elemental profiles of the selected states after DA heat treatment for 0.5h and 8h. The fcc matrix is represented by pink. Red arrows indicate the directions of 1D-elemental profiles acquired from cylindrical ROIs. (a) DA – 0.5h state showing the co-precipitation of Ni-Al and Co-Fe rich B2-precipitates at 33.7 at. % Co iso-surface and 21.2 at. % Al iso-surface. Black circles display Fe-enrichment and Al-depletion at the fcc/B2-NiAl interface. (b) DA – 0.5h state displaying the Al and Ni enrichment at sub-grain/cell boundaries in the absence of B2-precipitates. The interface between matrix and sub-grain/cell boundaries were represented at 16.9 at. % Al iso-surface and black dashed rectangle highlights the interface in 1D-elemental profiles. (c) DA – 8h state showing the evolution of Ni-Al and Co-Fe rich B2-precipitates at the end of 8h (33.6 at. % Co iso-surface, 12.1 at. % Al iso-surface and 33.6 at. % Ni iso-surface).

dislocation cell size nearly equals the primary dendrite arm spacing [14], and the resulting dislocation walls tend to align with interdendritic regions, where elements with low partitioning coefficients (k), such as Al ($k = 0.72$) and Ni ($k = 0.94$) in $Al_{10.5}Co_{25}Fe_{39.5}Ni_{25}$ MPEA [16], preferentially segregate during rapid solidification. Previous studies have shown that such enrichment can trigger the formation of B2-NiAl during solidification, potentially replacing cell boundaries by B2-NiAl that is interconnected through dislocation nano-bridges [50]. However, in $Al_{10.5}Co_{25}Fe_{39.5}Ni_{25}$ MPEA, the degree of Al and Ni supersaturation was insufficient to induce B2-NiAl formation on cell boundaries at this stage. This observation is consistent with our computational alloy design strategy (Fig. 1), which aimed at suppressing solidification-induced B2-NiAl formation in favor of controlled precipitation during aging. Hence, dislocations walls were observed to overlap with Al and Ni microsegregation at cell boundaries, as shown in Fig. 4**b**. These phenomena essentially brought local deviations into the phase stability between cell cores and cell boundaries due to the differences in local chemical driving forces and nucleation barriers for phase transformations, as schematically illustrated in Fig. 13**a**. Here, the cell boundaries were already enriched with Al and Ni, thereby holding a larger chemical driving force for precipitation of B2-NiAl phase (Fig. 1**c**). Additionally, dislocations are heterogeneous nucleation sites and thermodynamically desirable solute traps, which reduced the local nucleation barrier for phase transformations [46,47]. Thus, pipe

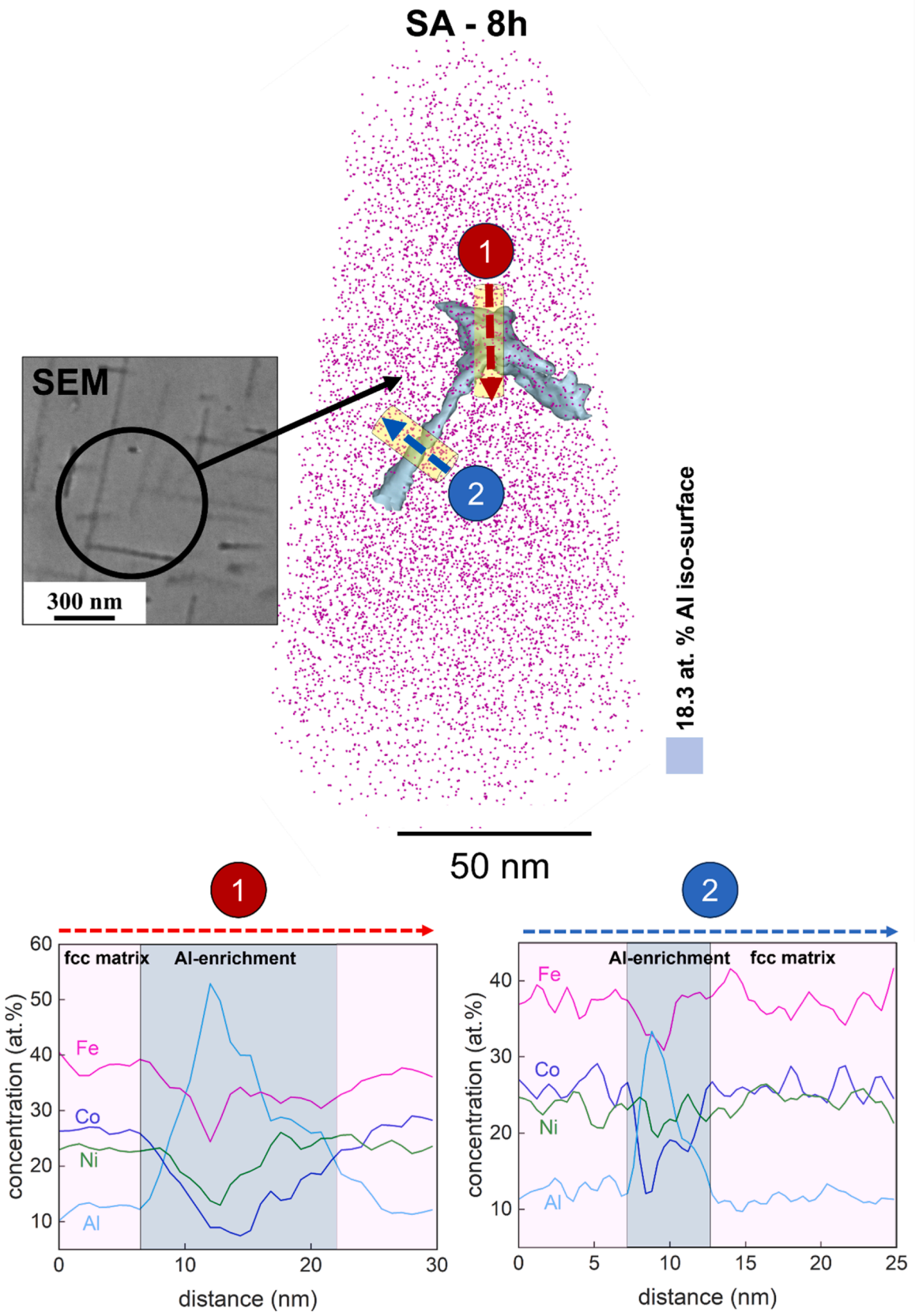

Fig. 10. APT analysis and respective 1D-elemental profiles of the needle-shaped precipitates in SA - 8h state extracted from RX grain. Analysis shows the Al concentration on the junction of two needle-shaped precipitates (1) and on the branch of the needle-shaped precipitate (2) (at 18.3 at. % Al iso-surface). The fcc matrix is represented by pink. Red and blue arrows display the directions of 1D-elemental profiles acquired from cylindrical ROIs.

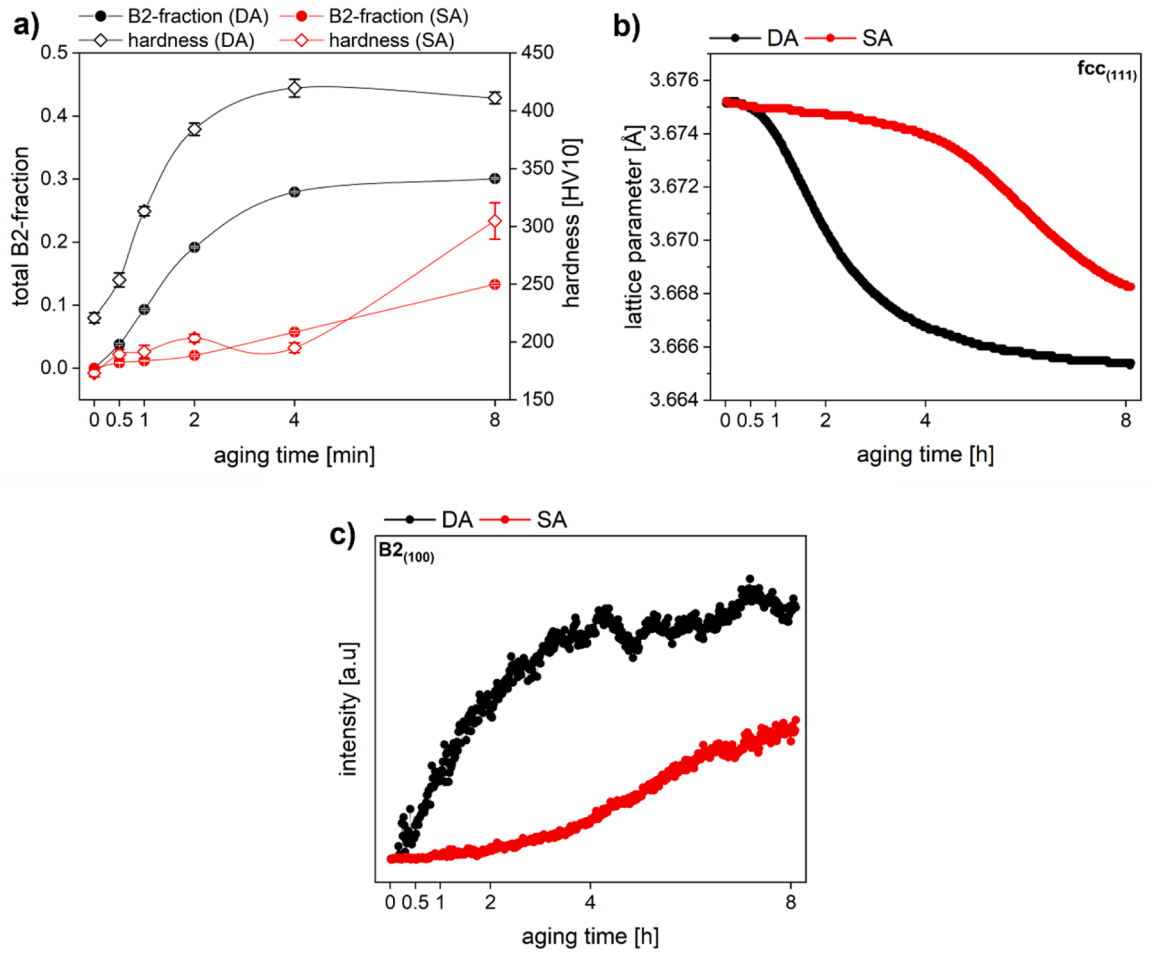

Fig. 11. (a) Evolution of total B2-fraction and hardness values. The B2-precipitate fractions were determined by Rietveld analysis employing GSAS II [64] software. (b-c) *In situ* SYXRD measurements acquired during aging of the as-built and solution annealed states at 700°C. (b) Lattice parameter change in the fcc phase. (c) Integrated intensity evolution of B2-precipitates. Changes in lattice parameter and integrated intensity were calculated through sequentially fitted single peaks.

Table 4
Dataset for measured B2-fractions and hardness values displayed in Fig. 11**a**.

State	Measured	aging duration at 700°C					
		0h	*0.5h*	*1h*	*2h*	*4h*	*8h*
DA	*total B2 [%]*	0	3.8 ± 0.2	9.3 ± 0.1	19.2 ± 0.2	27.9 ± 0.2	30.1 ± 0.2
	hardness [HV10]	221 ± 3	254 ± 6	313 ± 4	384 ± 5	420 ± 8	411 ± 5
SA	*total B2 [%]*	0	0.8 ± 0.1	1.1 ± 0.1	2.0 ± 0.2	5.7 ± 0.2	13.3 ± 0.2
	hardness [HV10]	173 ± 3	189 ± 4	192 ± 6	203 ± 3	194 ± 4	305 ± 16

diffusion of precipitate forming solutes that were abundant in these domains (e.g., Al) was favorable and accelerated through aging [70]. Accordingly, the cell boundaries served as nucleation sites for B2-NiAl (Fig. 7**a**), while depletion of Al and enrichment of Fe was observed at the interface of nucleating B2-NiAl precipitate and the fcc matrix (Fig. 9**a**). Since the B2-CoFe phase is thermodynamically stable at 700°C (Fig. 2**a**), enrichment of Fe at the interface of the nucleating B2-NiAl phase and the fcc matrix resulted in precipitation of B2-CoFe, followed by encapsulation of B2-CoFe by the B2-NiAl phase during growth, as schematically illustrated in Fig. 13**b**, and as observed experimentally (see Fig. 9**a**). It is important to note that while this encapsulation of B2-CoFe was revealed from APT analysis, some B2-precipitates with only Ni and Al enrichment were observed based on STEM-EDS (Fig. 7**a**). Moreover, the APT results of the DA - 0.5h state indicated that the composition of B2-NiAl and B2-CoFe phases were far from computationally predicted equilibrium (Table 4), as the excess Al and lower Ni concentration were observed in the former phase and lower Co concentration was observed in the latter phase. This can be related to the lower activation energy for Al diffusion in the fcc matrix and its acceleration by dislocations (e.g., pipe diffusion) [70], whereas the activation energies for, Co, Fe and Ni diffusion are higher [71]. When there are large differences in the diffusion rates of the precipitate-forming solutes, precipitates can grow faster by increasing the concentration of the fast-diffusing solute, e.g. Al as evidenced in Fig. 9**b**. This process resulted not only in far from equilibrium concentrations during precipitation [72], but also encapsulation of Co-Fe rich B2-precipitates due to fast diffusing Al-dominated concentration fields during the growth of B2-NiAl phase (Fig. 7). As aging continued, B2-NiAl and B2-CoFe co-precipitation decorated the cell boundaries, with minimal precipitation occurring within the cell cores at this stage of aging. Finally, co-precipitation of B2-NiAl and B2-CoFe emerged from cell boundaries towards cell cores and completely occupied the alloy matrix at the end of the aging treatment after 8h (Fig. 13**c**). Hence, the diffusion of solute atoms to the lattice defects during aging changed the local chemistry.

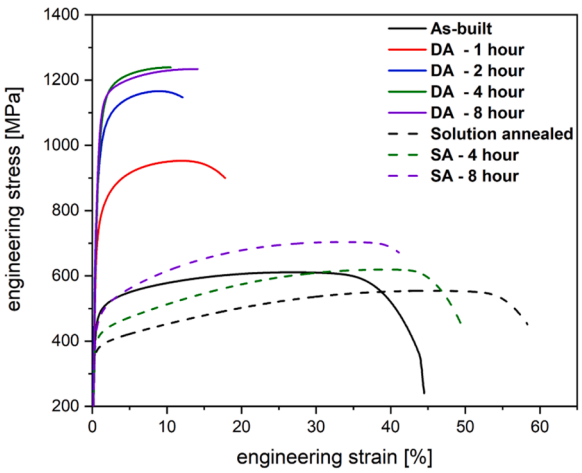

Fig. 12. (a) Engineering stress-strain curves of as-built, solution annealed, direct aging (DA) and solution annealing + aging (SA) states. The loading direction (TD) was parallel to the building direction (LD ∥ BD).

This change triggered site-specific phase transformations on cell boundaries by promoting the ordering of solute atoms into thermodynamically stable B2-NiAl and B2-CoFe phases.

For the solution annealed state, the precipitation behavior was distinctly different between RX and non-RX grains, as revealed by the local variations in density, size and morphology of precipitates (Fig. 6**g-k**). In the current study, the solution annealing temperature was sufficiently high to promote thermally activated softening mechanisms, i.e. static recovery and recrystallization. Both processes resulted in reduced dislocation densities via dislocation re-arrangement and annihilation (recovery) as well as nucleation and growth of new grains (recrystallization) [30,36,39] (Fig. 3**b**). However, microstructures obtained after PBF-LB/M tend to exhibit spatially varying degrees of dislocation densities, with regions displaying both low and high stored energies across different areas of the melt pools [2]. This results in uneven local driving forces for recrystallization throughout the as-built microstructure. These variations in plastic strains were evident from features in as-built microstructures such as differences in GOS, LAGB, and GND density maps (Fig. 3**a**). Consequently, although the cellular structures were annihilated, the combination of these effects led to heterogeneous/incomplete recrystallization. Some grains underwent complete recrystallization, while others exhibited static recovery, retaining a portion of LAGBs and GNDs.

During aging of the solution annealed state, sub-grain characteristics of RX and non-RX grains significantly affected the precipitation behavior. A similar co-precipitation mechanism was observed in non-RX grains, which retained a higher density of lattice defects (e.g., LAGBs) than RX grains (Fig. 3**b** and Fig 4**c**), but notably lower than those in the as-built condition (Fig. 3**a**). Moreover, dislocations in non-RX grains lacked the cellular arrangement present in the as-built state and appeared irregularly distributed (Fig. 4**c**). While lattice defects in non-RX grains still provided sufficient strain energy (as driving force for nucleation) and reduced the energy barrier for precipitation [70,73], the absence of cellular arrangement reduced the nucleation rate of precipitates, ultimately resulting in coarser precipitate morphologies and lower B2 volume fractions.

RX grains, on the other hand, possessed fewer defects that acted as nucleation sites, which in turn increases the interfacial and strain energy required for precipitation [43]. The precipitates in the RX grains exhibited high aspect ratios, with nearly perpendicular angles between the needle-shaped precipitates, as morphologically visible in Fig. 6**i-k**. Such morphological characteristics have previously been observed to originate from precipitates with common crystallographic orientations, as this arrangement reduces interfacial energy and consequently the total energy of the system [74,75]. Based on the 1D-elemental profiles in Fig. 10, the branches of the needle-shaped precipitates were rich in Al. This indicated that the needle-shaped precipitates were far from their equilibrium composition of thermodynamically stable B2-NiAl after aging for 8h (Table 4), and there were no precursors for the co-precipitation of B2-CoFe phase, contrary to the non-RX grains. The formation of Al-rich needles prior to the thermodynamically stable phases is governed by diffusion kinetics, as Al exhibits the lowest activation energy and highest diffusivity compared to Ni, Co, and Fe. These observations are consistent with reported literature on high-entropy alloys, which suggests that intermediate precipitate compositions enriched in the fastest-diffusing element evolve first [76,77]. Interestingly, the junction points of needle-shaped precipitates revealed significant enrichment in Al, where concentration reached up to ~53 at. % (Fig. 10). Previous studies [78,79] have demonstrated that the anisotropic diffusion fields of growing needle-shaped precipitates can interact, leading to either soft or hard impingement well before the equilibrium volume fraction is achieved. Soft impingement occurs when the diffusion fields or concentration gradients of nearby precipitates begin to overlap, without the precipitates themselves making physical contact. In contrast, hard impingement takes place when the precipitates grow until they physically intercept one another. In Fig. 6**k**, examples of both soft and hard impinged precipitates were visible. In the case of hard impingement, where precipitates come into contact, compositional clustering or localized changes in composition may develop at the contact points, as seen in Fig. 10, as the intercepting precipitates can alter the overall composition [74].

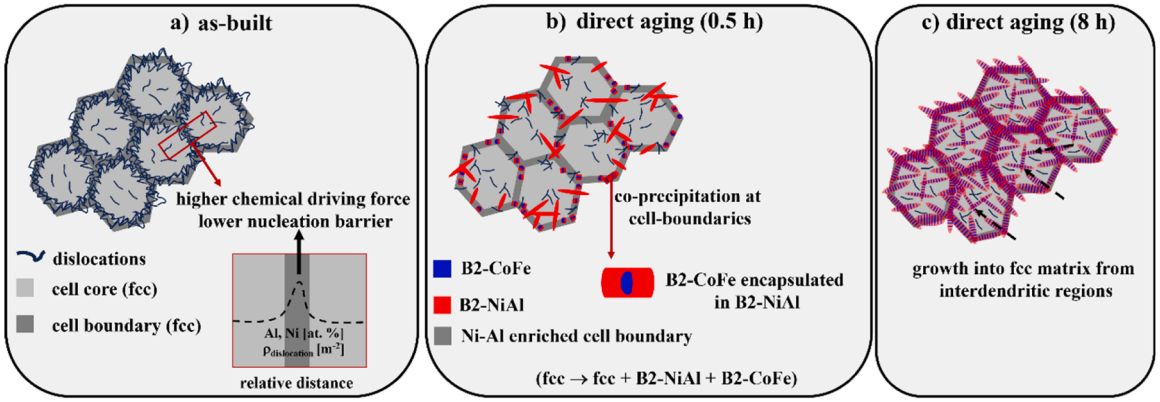

Fig. 13. Schematic illustration of site-specific co-precipitation of B2-NiAl and B2-CoFe phases at cell boundaries based on STEM-EDS and APT analyses.

5.2. Effect of microstructural heterogeneities on precipitation kinetics

To understand the differences in precipitation kinetics between the as-built and solution annealed states, it is essential to consider the combined influence of microstructural heterogeneities. For instance, dislocations can move during annealing and act as solute-collecting domains. This behavior promotes the local enrichment of solute atoms at dislocations and accelerates the overall precipitation process [80]. In the as-built state, the dislocation densities were larger, and dislocation cells also exhibited microsegregation of Al and Ni along the cell boundaries. Previous studies in AM Ni-based superalloys have demonstrated that microsegregation was responsible for accelerating the precipitation kinetics by reducing the nucleation barrier for phase transformation [26, 81]. Additionally, in regions with a higher dislocation density and localized concentrations of Al and Ni, no long-range diffusion of these elements was required to initiate phase transformations.

Hence, in the as-built state, the abundance of nucleation sites due to the presence of cellular structures initially resulted in a rapid increase in the fraction of B2-precipitates. This was reflected in the shrinkage of the fcc lattice and the rise in integrated $B2_{(100)}$ intensities, which occurred drastically within the first 2h of aging (Fig. 11**b**). During this phase, many precipitates were formed (e.g., 63.5% of the final precipitate volume fraction, Table 4), particularly at dislocations and Ni-Al rich cell boundaries (Fig. 5**a-c** and Fig. 6**a-c**). As precipitates began to grow from the cell boundaries into the cell core, the lattice parameter decreased more gradually (2-4h), suggesting a slower precipitation rate as the fcc-matrix started to become depleted of solute atoms. As aging continued, the number of available diffusion and nucleation sites became almost saturated, having already facilitated the precipitation [74]. Peak hardness was reached after 4h, coinciding with a saturation phase (4-8h), where changes in the fcc lattice parameter were minimal. This indicated that the system was approaching equilibrium (Table 3, Fig. 9), with little additional solute being absorbed into the precipitates. Moreover, the abundance of effective nucleation sites also influenced the precipitate size. Numerous nuclei formed rapidly by enhanced solute diffusion, which distributed the available solutes among many sites and limited the growth of each individual precipitate. Ultimately, this frequent nucleation coupled with constrained growth produced a finer precipitate size compared to SA state at the end of DA.

In contrast, the solution annealed state, with its reduced density of microstructural heterogeneities and absence of cellular structures, exhibited slower solute removal from the fcc matrix. The slower precipitation rate, reflected in moderate changes in lattice parameters during the first 4h (Fig. 11**b**), was due to fewer nucleation sites and diffusion paths. Although the onset of precipitation was not delayed, as can be seen in Fig. 5**d-f**, the growth of B2-precipitates accelerated during further aging, indicating that the matrix retained solute atoms for a longer time. Therefore, a steeper drop in the lattice parameter occurred only after a critical number of precipitates had formed (when the phase boundary diffusion became dominant), which happened later in the SA state due to the lower initial density of defects available to facilitate nucleation and growth of precipitates. Thus, the main reason for the accelerated precipitation kinetics in the as-built state was primarily due to the synergistic effects of chemical heterogeneity in cellular structures, defect-mediated segregation and diffusion [43,70,82,83], whereas reduction of such features in SA state resulted in lower precipitation rates.

5.3. Correlation between microstructure and mechanical properties

5.3.1. Initial states

Microstructural heterogeneities not only influenced the phase transformation behavior but also the mechanical response (Fig. 12, **Table S1**). Considering distinct microstructural characteristics of each state, the contributions of multiple strengthening mechanisms to the yield strength of the material were calculated and the results are

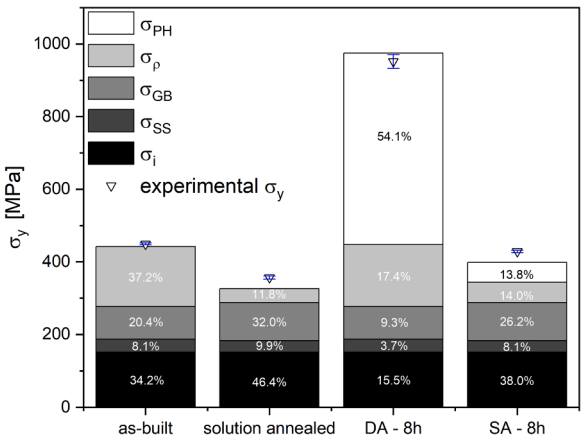

Fig. 14. Comparison between calculated and experimental yield strength (σ_y) of $Al_{10.5}Co_{25}Fe_{39.5}Ni_{25}$ alloy in different conditions. Numbers in the bars indicate the contribution of each individual strengthening mechanism to the total σ_y.

summarized in Fig. 14. The room temperature yield strength was estimated based on the summation of individual strengthening contributions according to the following equation:

$$\sigma_y = \sigma_i + \sigma_{SS} + \sigma_{GB} + \sigma_\rho + \sigma_{PH} \quad (1)$$

where σ_i is the friction stress, σ_{SS} is the solid solution strengthening, σ_{GB} is the grain boundary strengthening, σ_ρ is the dislocation strengthening, and σ_{PH} is the precipitation strengthening. Since both initial states were free of precipitates, the contribution of σ_{PH} was neglected. Here, σ_i was adapted from the compositionally similar $Al_{0.3}CoFeNi$ alloy and considered as 151.2 MPa for both states [84]. The conventional methods for determining solid solution strengthening were employed [85], as the $Al_{10.5}Co_{25}Fe_{39.5}Ni_{25}$ MPEA can be considered as CoFeNi solvent matrix with Al as a solute [86]. Hence, σ_{SS} was determined based on elastic interactions between dislocations and solute atoms using following formula [85–87]:

$$\sigma_{SS} = M\frac{G\varepsilon_s^{3/2}c^{1/2}}{700} \quad (2)$$

where G is the shear modulus of CoFeNi and taken as 60 GPa [88,89]. The Taylor factor (M) was calculated using the MTEX toolbox in MATLAB based on EBSD data. All fcc slip systems were considered, and a deformation gradient tensor corresponding to uniaxial tension along the BD was applied. The mean crystallographic orientation of each grain (∥ BD) within the field of view (Fig. 3) was determined. Using these orientations, the Taylor factor was computed for each grain and subsequently averaged across the entire area using an area-weighted approach. The resulting M values were 3.24 for the as-built condition and 3.12 for the solution-annealed state. Additionally, c represents the total molar ratio of Al in CoFeNi fcc matrix, whereas ε_s is the interaction parameter, namely,

$$\varepsilon_s = \left|\frac{\varepsilon_G}{1+0.5\varepsilon_G} - 3\varepsilon_a\right| \quad (3)$$

and ε_G and ε_a are elastic and atomic size mismatches and described as:

$$\varepsilon_G = \frac{1}{G}\frac{dG}{dc} \quad (4)$$

$$\varepsilon_a = \frac{1}{a}\frac{da}{dc} \quad (5)$$

where a is the lattice parameter of the CoFeNi fcc matrix and taken as 3.5690 Å [90] to calculate ε_a, whereas ε_G is negligible in comparison to

ε_a. The lattice parameters of as-built and solution annealed states were obtained from SYXRD data. Therefore, the contribution of σ_{SS} was determined to be 35.9 MPa for as-built state and 32.2 MPa for solution annealed state. The low value of σ_{SS} implies that solid solution strengthening was not one of the dominant strengthening mechanisms. The grain boundary strengthening effect σ_{GB} was evaluated by the Hall-Petch relationship:

$$\sigma_{GB} = k \cdot d^{-0.5} \quad (6)$$

Here the d represents the effective average grain size (d_{eff}= 190 μm for as-built state, d_{eff}= 142.6 μm for solution annealed state), calculated from EBSD data using MATLAB toolbox MTEX. This value represents the average mean equivalent grain diameter, obtained from distributions based on area and number fractions to effectively describe the size of grains with elongated morphologies [91]. k is the Hall-Petch parameter and was selected as 1244 $MPa\sqrt{\mu m}$ according to studies conducted on the compositionally similar $Al_{0.3}$CoFeNi alloy [84]. σ_{GB} was found to be 90.2 MPa for as-built state and 104.1 MPa for solution annealed state. Lastly, contribution of σ_ρ was investigated by applying Taylor hardening law:

$$\sigma_\rho = \alpha \cdot M \cdot G \cdot b \cdot \sqrt{\rho} \quad (7)$$

Here, the dislocation interaction factor α was 0.2 and M was calculated from EBSD data. The reported shear modulus, G, for quaternary and higher-order high-entropy alloys ranges from 74 to 88 GPa [86–90,92–94]. Consequently, G was adopted as 76.9 GPa from the Al-added Cantor Alloy ($Al_{0.1}$CoCrFeMnNi). A burgers vector (b) of 0.257 nm was selected and dislocation density is depicted by ρ. As established in prior studies on deformed fcc metals [95–98], dislocation cell substructures often exhibit an empirical relationship between the cell diameter d_c and the bulk dislocation density ρ:

$$\rho = \frac{200}{\pi \cdot dc2} \quad (8)$$

This correlation has also been shown to hold for fcc AM alloys [95]. Following this framework, the dislocation density in the as-built condition was initially estimated using the measured d_c from STEM images (Fig. 4**b**). The average d_c in the as-built condition was 578 ± 53 nm, yielding dislocation densities of 2.31 × 10^{14} m^{-2} and 1.60 × 10^{14} m^{-2} for the lower (525 nm) and upper (631 nm) bounds of the standard deviation, respectively. The mean dislocation density calculated from the average d_c was 1.85 × 10^{14} m^{-2}. For comparison, ρ was also determined from SYXRD data to capture the influence of both GND and statistically stored dislocation (SSDs) densities. ρ was calculated using the Williamson-Hall method [99,100], based on the relationship given by $\rho = 2\sqrt{3}\varepsilon / db$ [86,94], where b is burgers vector, ε is the microstrain and d is the crystallite size estimated from the SYXRD. The SYXRD based value of ρ was 1.65 × 10^{14} m^{-2} for the as-built state and 8.66 × 10^{13} m^{-2} for the solution annealed state. The ρ of as-built state lies well within the range obtained from the equation *(8)*, confirming good agreement between two approaches. Therefore, to ensure consistent and comparable analysis across all states (e.g., dislocation cells are only present in as-built state), ρ derived from SYXRD were used to evaluate contribution of σ_ρ for all states. While calculating the σ_ρ of the solution annealed state, only the fraction of the non-RX grains ($f_{non-RX} = 0.335$) were considered [101]. Therefore, the Taylor equation for solution annealed state can be written as:

$$\sigma_{\rho s} = f_{non-RX} \cdot \alpha \cdot M \cdot G \cdot b \cdot \sqrt{\rho} \quad (9)$$

Based on the previous equations, σ_ρ was calculated as 164.5 MPa and 38.4 MPa for the as-built and solution annealed states, respectively. Summation of the individual strengthening contributions yielded in σ_y of 441.9 MPa with σ_ρ contributing the largest share (~37.2%) followed by σ_i (~34.2%) for the as-built state . In contrast, σ_y of the solution annealed state was calculated to be 326 MPa, with σ_i (~46.4 %) providing the main contribution and σ_{GB} accounting for ~32.0%. Calculated values closely matched the experimentally measured yield strengths of 449.2 ± 2.5 and 356.7 ± 4.5 MPa for as-built and solution annealed state, respectively (Fig. 14). Considering all contributions, the primary difference stems from the initially higher dislocation densities in the as-built state, which increased dislocation interactions and resistance to dislocation motion during deformation. Hence, as numerous studies have shown, presence of cellular structures led to a notable change in mechanical properties, particularly contributing to an increase in yield strength [13,17–19,92,102,103].

5.3.2. Heat treated states

As shown in Fig. 5 and Fig. 6, both DA and SA heat treatments led to the formation of incoherent B2-precipitates that were expected to induce hardening to varying degrees between the states. This hardening inevitably increased the yield strength but at the cost of ductility, resulting in a strength-ductility trade-off (Fig. 12). Here, we focused our comparisons on the DA-8h and SA-8h states to explore how the differences in precipitate size, volume fraction and distribution contributed to increase in yield strength over the extended aging times.

For heat treated states, the friction stress σ_i, solid solution strengthening (σ_{ss}) and grain boundary strengthening (σ_{GB}) were assumed to remain unchanged from their counterparts before aging, as the nominal composition and effective grain size of the fcc phase were not altered by the heat treatments. Therefore, the primary difference in hardening behavior is attributed to changes in dislocation strengthening and introduction of precipitates. The formation of B2-precipitates anticipated to increase dislocation density due to GNDs, elastic strain fields and misfit dislocations caused by lattice mismatch with the fcc matrix [104]. As precipitates nucleate and grow from cell boundaries to cell cores, they impose local strains due to volume change and coherency loss. This can drive dislocation generation or migration into dislocation-free regions, such as cell interiors, as observed from STEM images in Fig. 7. Thus, as the precipitate volume fraction increases with aging time, more dislocations are generated at the B2-interfaces to accommodate the misfit [105,106]. This suggestion is also supported by the FWHM evolution in the fcc phase (**Fig. S7**), where FWHM increased relative to the initial states at the end of the aging, with the SA heat treatment showing the highest FWHM value after 8h. Hence, equation (8) can be used to calculate the contribution of dislocation strengthening σ_ρ. For the DA – 8h sample, ρ was 1.76 × 10^{14} m^{-2}, slightly higher than the as-built state, which aligned with the FWHM evolution in **Fig. S7.** This resulted in a σ_ρ contribution of 169.9 MPa for DA – 8h state. For the SA-8h state, large B2-precipitates were primarily located within non-RX grains, while RX grains exhibit only a minimal volume fraction (Fig. 6**g-k**). Since dislocation generation and the associated strengthening effects are expected to be more significant where larger precipitates are present, our analysis solely considered the non-RX grains as the host of misfit dislocations. Hence, equation (9) can be used to calculate the contribution of dislocation strengthening $\sigma_{\rho s}$. Consequently, ρ of SA – 8h state was 1.83 × 10^{14} m^{-2}, consistent with the observation in **Fig. S7**, leading to a contribution from $\sigma_{\rho s}$ of 55.9 MPa.

Hardening by precipitation occurs through either a particle shearing mechanism or a dislocation bypassing mechanism (Orowan-type). A bypassing mechanism typically occurs when the precipitate size exceeds a critical threshold or when the precipitates are semi-coherent or incoherent with the matrix. In current study, the B2-phases showed high lattice mismatch (~20%) and incoherent relationship with the fcc matrix [50]. Based on the current precipitate size and crystal structure, the Orowan mechanism is expected to be active. Therefore, a precipitation strengthening model was proposed to correlate the size and volume fraction of B2-precipitates with the yield strength of the DA-8h and SA-8h states [107,108] using equations (10) and (11). Since the B2-precipitates exhibited an intricate and interconnected morphology with high aspect ratios, the precipitates were assumed as elliptical to simplify the calculations. To this end, their mean circular equivalent

radius (r) was approximated through ellipse fitting. The r of B2-precipitates was determined to be 128.1 nm and 180.6 nm for DA – 8h state and SA- 8h state, respectively. For non-shearable B2-precipitates, the effective obstacle spacing is defined as the center-to-center distance between precipitates, L, which can be expressed as:

$$L = 2\sqrt{\frac{2}{3}}r\left(\sqrt{\frac{\pi}{4f}} - 1\right) \tag{10}$$

Here, r is the mean circular equivalent radius of B2-precipitates and f is the total volume fraction of B2-precipitates acquired via SYXRD (Table 3). Thus, contribution of the precipitates to yield strength σ_y is given by:

$$\sigma_{PH} = M \cdot \frac{0.4Gb}{\pi\sqrt{1-\nu}} \cdot \frac{ln\left(2\sqrt{\frac{2}{3}}r \Big/ b\right)}{L} \tag{11}$$

where, ν is the Poisson's ratio and taken as 0.3 [93]. The Taylor factor M, the Burgers vector b and the shear modulus G was assumed to be identical to the previously used values. By substituting all values into equations (10) and (11), the precipitation strengthening contribution σ_{PH} for DA – 8h state was determined to be 527.7 MPa, accounting for ~54.1% of the total yield strength and identifying it as the major strengthening mechanism. For the SA – 8h state equation (11) was modified because the larger B2-preciptates responsible for strengthening were observed solely in non-RX grains. Hence precipitation strengthening σ_{PHS} for SA – 8h state can be written as:

$$\sigma_{PHS} = f\text{non} - \text{RX} \cdot M \cdot \frac{0.4Gb}{\pi\sqrt{1-\nu}} \cdot \frac{ln\left(2\sqrt{\frac{2}{3}}r \Big/ b\right)}{L} \tag{12}$$

where $f_{non\text{-}RX}$ is the fraction of non-RX (0.335) grains in the microstructure. Introducing all values, σ_{PHS} contribution for the SA – 8h state was found to be 54.9 MPa or ~13.8% of the total yield strength. Summing up all the strengthening contributions resulted in a yield strength σ_y of 974.9 MPa for the DA-8h, which was very close to the experimentally observed value of 951.8 ± 19.0 MPa. Similarly, for the SA-8h state, the calculated yield strength σ_y was 398.3 MPa, aligning well with the experimentally observed value of 428.7 ± 3.5 MPa.

Although several calculation parameters were estimated, such as assuming the spherical morphologies for precipitates, the analysis clearly identified the factors responsible for changes in mechanical properties. This outcome demonstrated that the approach effectively captured the key mechanisms despite the inherent approximations. Therefore, based on the calculated values for the strengthening mechanisms (Fig. 14), the primary difference between the DA – 8h and SA-8h state originated from the disparity in precipitation strengthening contribution. In the DA-8h state, the cellular structure mediated precipitation provided higher volume fraction of precipitates, lower mean precipitate radius and shorter effective obstacle spacing and restricted dislocation mobility by acting as strong barriers. The relatively uniform distribution of these obstacles compared to the SA-8h state provided consistent resistance to dislocation motion, leading to significantly enhanced strength upon deformation. In contrast, the SA state displayed non-uniform precipitation behavior between RX and non-RX grains. Previous studies demonstrated that strain was preferentially partitioned to softer domains (e.g., RX grains), while harder domains (e.g., non-RX grains) generated back-stresses that delayed yielding and enhanced strain hardening in the softer domains [109–111]. The RX grains (accounting to 66.5% of total grains based on EBSD analysis), which contained a lower fraction of B2-precipitates and lacked larger ones, were softer and more easily deformed. This resulted in plastic strain partitioning in RX-grains that significantly enhanced plasticity by avoiding strain localization [112–114], as evidenced by the SA-8h state's low yield strength and high work hardening capability (Fig. 12).

6. Summary and conclusions

In this study, $Al_{10.5}Co_{25}Fe_{39.5}Ni_{25}$ multi-principal element alloy (MPEA) was computationally designed to exploit cellular structures that formed as a product of the process-inherent conditions during laser powder bed fusion (PBF-LB/M) additive manufacturing (AM). The alloy design and selection were based on segregation of Al (a fast-diffusing, precipitate-forming element) at the interdendritic regions during solidification. By this way, solute segregation was intentionally organized to overlap with dislocations at the cell boundaries. This outcome gave the possibility to utilize the differences in chemical driving forces and nucleation barriers for precipitation between the cell cores and cell boundaries through direct aging (DA). To investigate the effect of cellular structures on the microstructure evolution and mechanical properties, a reference state was introduced by eliminating the cellular structures via solution annealing prior to aging (SA). The results indicated the following:

1 Multi-scale microstructure characterization showed that cell boundaries displayed a high density of dislocations as well as enrichment of Al and Ni solutes that aligned with the intended alloy design strategy. The structure of cell boundaries enhanced solute diffusion and facilitated phase transformation, promoting the site-specific co-precipitation of B2-NiAl and B2-CoFe phases. Al-diffusion was the dominating factor in controlling precipitation, owing to its lower activation energy for diffusion compared to other substitutional solutes.
2 The cellular structures delivered a high number of nucleation sites while defect-induced solute segregation during aging led to a faster precipitation rate. These phenomena driven by cellular structures ensured higher volume fraction of precipitates, finer precipitate size, and smaller precipitate spacing that resulted in a microstructure that combines high yield strength, while still showing considerable amount of ductility after 8h of aging.
3 The absence of cellular structures in the SA state resulted in slower solute depletion from the face centered cubic (fcc) matrix, which inhibited early-stage co-precipitation of B2-NiAl and B2-CoFe phases during aging. Non-recrystallized (non-RX) grains still showed B2-NiAl and B2-CoFe co-precipitation, while lower fraction of B2-precipitates and coarser precipitate size were observed compared to its DA counterpart. The recrystallized (RX) grains displayed needle-shaped Al-enriched precipitates with high aspect ratios. This evidence showed the dramatic difference in phase transformation behavior resulting from the absence of cellular structures.
4 The non-uniform characteristics of precipitates in RX and non-RX grains in SA state led to a higher ductility but a lower yield strength, despite the 8h of aging.

We emphasize that our approach can be considered when designing new precipitation strengthened alloys for AM. The precipitation behavior can be finely tuned by pairing the precipitate forming elements with high density of dislocations that stem from layer-by-layer production during AM. Our study clearly demonstrated that with suitable heat treatments, solute diffusion within these domains can be facilitated to tailor nano- and microstructures, enhancing the mechanical properties of AM alloys. The future focus should lie on developing alloy-design strategies that leverage cellular structures, which can enable the design of advanced alloys without the need for energy-intensive homogenization or multi-step annealing.

CRediT authorship contribution statement

Ahmet Turnali: Writing – review & editing, Writing – original draft, Visualization, Software, Methodology, Investigation, Formal analysis,

Data curation, Conceptualization. **Avinash Hariharan:** Writing – review & editing, Visualization, Investigation, Formal analysis. **Efthymios Polatidis:** Writing – review & editing, Investigation, Formal analysis, Data curation. **Nicolas J. Peter:** Writing – review & editing, Investigation. **Jaqueline Gehlmann:** Investigation. **Christos Sofras:** Investigation. **Zoltan Hegedüs:** Writing – review & editing, Investigation. **Lennart Sayk:** Investigation. **Tarek Allam:** Writing – review & editing. **Johannes Henrich Schleifenbaum:** Resources. **Christian Haase:** Writing – review & editing, Supervision, Funding acquisition, Conceptualization.

Declaration of competing interest

The authors declare that they have no known competing financial interests or personal relationships that could have appeared to influence the work reported in this paper.

Acknowledgements

This work was funded by the German Federal Ministry of Education and Research (BMBF) as part of the NanoMatFutur project "MatAM - Design of Additively Manufactured High-Performance Alloys for Automotive Applications" (Project ID: 03XP0264) and from the European Research Council (ERC) under the European Union's Horizon Europe research and innovation program (grant agreement No. 101077977 HeteroGenius4D). The study contains results from experiments done at the Ernst Ruska Centre (ER-C) for Microscopy and Spectroscopy with Electrons at Forschungszentrum Jülich (FZJ) in Germany [https://doi.org/10.17815/jlsrf-2–68, https://doi.org/10.17815/jlsrf-2–106]. Access to beamtime at the ER-C was provided through the DFG Core Facility Project (FZJ_IEK2_PN1). The authors also wish to acknowledge the Deutsches Elektronen-Synchrotron (DESY, Hamburg, Germany), a member of the Helmholtz Association (HGF), for providing experimental facilities. Beamtime at DESY was allocated for proposal I-20220679 EC. Additionally, the authors thank Jan-Philipp Roth from the University of Applied Sciences Osnabrück, Germany, for his support in atomizing the $Al_{10.5}Co_{25}Fe_{39.5}Ni_{25}$ alloy powder used in this study.

Supplementary materials

Supplementary material associated with this article can be found, in the online version, at doi:10.1016/j.actamat.2025.121423.

References

[1] B. Guo, D. Cui, Q. Wu, Y. Ma, D. Wei, S R K L, et al., Segregation-dislocation self-organized structures ductilize a work-hardened medium entropy alloy, Nat. Commun. 16 (1) (2025) 1475, https://doi.org/10.1038/s41467-025-56710-3.
[2] S. Gao, Z. Li, S. van Petegem, J. Ge, S. Goel, J.V. Vas, et al., Additive manufacturing of alloys with programmable microstructure and properties, Nat. Commun. 14 (1) (2023) 6752, https://doi.org/10.1038/s41467-023-42326-y.
[3] A. Hariharan, M. Ackermann, S. Koss, A. Khosravani, J.H. Schleifenbaum, P. Köhnen, et al., High-Speed 3D Printing Coupled with Machine Learning to Accelerate Alloy Development for Additive Manufacturing, Adv. Sci. (Weinh) (2025) e2414880, https://doi.org/10.1002/advs.202414880.
[4] Y. Li, D. Gu, Parametric analysis of thermal behavior during selective laser melting additive manufacturing of aluminum alloy powder, Mater. Des. 63 (2014) 856–867, https://doi.org/10.1016/j.matdes.2014.07.006.
[5] M.V. Pantawane, Y-H Ho, S.S. Joshi, NB. Dahotre, Computational Assessment of Thermokinetics and Associated Microstructural Evolution in Laser Powder Bed Fusion Manufacturing of Ti6Al4V Alloy, Sci. Rep. 10 (1) (2020) 7579, https://doi.org/10.1038/s41598-020-63281-4.
[6] S.A. Khairallah, A.T. Anderson, A. Rubenchik, WE. King, Laser powder-bed fusion additive manufacturing: Physics of complex melt flow and formation mechanisms of pores, spatter, and denudation zones, Acta Mater. 108 (2016) 36–45, https://doi.org/10.1016/j.actamat.2016.02.014.
[7] T. DebRoy, H.L. Wei, J.S. Zuback, T. Mukherjee, J.W. Elmer, J.O. Milewski, et al., Additive manufacturing of metallic components – Process, structure and properties, Prog. Mater. Sci. 92 (2018) 112–224, https://doi.org/10.1016/j.pmatsci.2017.10.001.
[8] W.J. Sames, F.A. List, S. Pannala, R.R. Dehoff, SS. Babu, The metallurgy and processing science of metal additive manufacturing, Int. Mater. Rev. 61 (5) (2016) 315–360, https://doi.org/10.1080/09506608.2015.1116649.
[9] Y.M. Wang, T. Voisin, J.T. McKeown, J. Ye, N.P. Calta, Z. Li, et al., Additively manufactured hierarchical stainless steels with high strength and ductility, Nat. Mater. 17 (1) (2018) 63–71, https://doi.org/10.1038/nmat5021.
[10] P.C. Collins, D.A. Brice, P. Samimi, I. Ghamarian, HL. Fraser, Microstructural Control of Additively Manufactured Metallic Materials, Annu Rev. Mater. Res. 46 (1) (2016) 63–91, https://doi.org/10.1146/annurev-matsci-070115-031816.
[11] D. Herzog, V. Seyda, E. Wycisk, C. Emmelmann, Additive manufacturing of metals, Acta Mater. 117 (2016) 371–392, https://doi.org/10.1016/j.actamat.2016.07.019.
[12] WE. Frazier, Metal Additive Manufacturing: A Review, J. of Materi Eng and Perform 23 (6) (2014) 1917–1928, https://doi.org/10.1007/s11665-014-0958-z.
[13] D. Kong, C. Dong, S. Wei, X. Ni, L. Zhang, R. Li, et al., About metastable cellular structure in additively manufactured austenitic stainless steels, Addit. Manuf. 38 (2021) 101804, https://doi.org/10.1016/j.addma.2020.101804.
[14] K.M. Bertsch, G. Meric de Bellefon, B. Kuehl, D.J. Thoma, Origin of dislocation structures in an additively manufactured austenitic stainless steel 316L, Acta Mater. 199 (2020) 19–33, https://doi.org/10.1016/j.actamat.2020.07.063.
[15] G. Wang, H. Ouyang, C. Fan, Q. Guo, Z. Li, W. Yan, et al., The origin of high-density dislocations in additively manufactured metals, Mater. Res. Lett. 8 (8) (2020) 283–290, https://doi.org/10.1080/21663831.2020.1751739.
[16] A. Turnali, D. Kibaroglu, N. Evers, J. Gehlmann, L. Sayk, N.J. Peter, et al., Segregation-guided alloy design via tailored solidification behavior, Mater. Today Adv. 25 (2025) 100549, https://doi.org/10.1016/j.mtadv.2024.100549.
[17] D. Kong, C. Dong, X. Ni, Z. Liang, C. Man, X. Li, Hetero-deformation-induced stress in additively manufactured 316L stainless steel, Mater. Res. Lett. 8 (10) (2020) 390–397, https://doi.org/10.1080/21663831.2020.1775149.
[18] Z.G. Zhu, Q.B. Nguyen, F.L. Ng, X.H. An, X.Z. Liao, P.K. Liaw, et al., Hierarchical microstructure and strengthening mechanisms of a CoCrFeNiMn high entropy alloy additively manufactured by selective laser melting, Scr. Mater. 154 (2018) 20–24, https://doi.org/10.1016/j.scriptamat.2018.05.015.
[19] Y-K Kim, J. Choe, K-A. Lee, Selective laser melted equiatomic CoCrFeMnNi high-entropy alloy: Microstructure, anisotropic mechanical response, and multiple strengthening mechanism, J. Alloys. Compd. 805 (2019) 680–691, https://doi.org/10.1016/j.jallcom.2019.07.106.
[20] J.M. Park, H. Kwon, J. Choe, K.T. Kim, J-H Yu, Y-U Heo, et al., Cell boundary engineering of ferrous medium-entropy alloy fabricated by laser powder bed fusion, Scr. Mater. 237 (2023) 115715, https://doi.org/10.1016/j.scriptamat.2023.115715.
[21] T. Pinomaa, M. Lindroos, M. Walbrühl, N. Provatas, A. Laukkanen, The significance of spatial length scales and solute segregation in strengthening rapid solidification microstructures of 316L stainless steel, Acta Mater. 184 (2020) 1–16, https://doi.org/10.1016/j.actamat.2019.10.044.
[22] T.R. Smith, J.D. Sugar, C. San Marchi, J.M. Schoenung, Strengthening mechanisms in directed energy deposited austenitic stainless steel, Acta Mater. 164 (2019) 728–740, https://doi.org/10.1016/j.actamat.2018.11.021.
[23] W.K. Choo, J.H. Kim, J.C. Yoon, Microstructural change in austenitic Fe-30.0wt% Mn-7.8wt%Al-1.3wt%C initiated by spinodal decomposition and its influence on mechanical properties, Acta Mater. 45 (12) (1997) 4877–4885, https://doi.org/10.1016/S1359-6454(97)00201-2.
[24] P. Köhnen, M. Létang, M. Voshage, J.H. Schleifenbaum, C. Haase, Understanding the process-microstructure correlations for tailoring the mechanical properties of L-PBF produced austenitic advanced high strength steel, Addit. Manuf. 30 (2019) 100914, https://doi.org/10.1016/j.addma.2019.100914.
[25] C. Kumara, A.R. Balachandramurthi, S. Goel, F. Hanning, J. Moverare, Toward a better understanding of phase transformations in additive manufacturing of Alloy 718, Materialia (Oxf) 13 (2020) 100862, https://doi.org/10.1016/j.mtla.2020.100862.
[26] F. Zhang, L.E. Levine, A.J. Allen, M.R. Stoudt, G. Lindwall, E.A. Lass, et al., Effect of heat treatment on the microstructural evolution of a nickel-based superalloy additive-manufactured by laser powder bed fusion, Acta Mater. 152 (2018), https://doi.org/10.1016/j.actamat.2018.03.017.
[27] Y. Yao, L. Fan, R. Ding, C. Franke, Z. Yang, W. Liu, et al., On the role of cellular microstructure in austenite reversion in selective laser melted maraging steel, J. Mater. Sci. Technol. 184 (2024) 180–194, https://doi.org/10.1016/j.jmst.2023.10.032.
[28] Y. Zhao, K. Li, M. Gargani, W. Xiong, A comparative analysis of Inconel 718 made by additive manufacturing and suction casting: Microstructure evolution in homogenization, Addit. Manuf. 36 (2020) 101404, https://doi.org/10.1016/j.addma.2020.101404.
[29] J.M. Park, E.S. Kim, H. Kwon, P. Sathiyamoorthi, K.T. Kim, J-H Yu, et al., Effect of heat treatment on microstructural heterogeneity and mechanical properties of 1% C-CoCrFeMnNi alloy fabricated by selective laser melting, Addit. Manuf. 47 (2021) 102283, https://doi.org/10.1016/j.addma.2021.102283.
[30] V.P. Narayana Samy, F. Brasche, I. Šulák, B. Verma, B. Nowak, Z. Chlup, et al., The influence of microstructural heterogeneities on high-temperature mechanical properties of additively manufactured γ'-forming Ni-based alloys, Addit. Manuf. 88 (2024) 104267, https://doi.org/10.1016/j.addma.2024.104267.
[31] S.A. Mantri, S. Dasari, A. Sharma, T. Alam, M.V. Pantawane, M. Pole, et al., Effect of micro-segregation of alloying elements on the precipitation behaviour in laser surface engineered Alloy 718, Acta Mater. 210 (2021) 116844, https://doi.org/10.1016/j.actamat.2021.116844.
[32] T. Allam, K.G. Pradeep, P. Köhnen, A. Marshal, J.H. Schleifenbaum, C. Haase, Tailoring the nanostructure of laser powder bed fusion additively manufactured

maraging steel, Addit. Manuf. 36 (2020) 101561, https://doi.org/10.1016/j.addma.2020.101561.
[33] X. Li, J.J. Shi, C.H. Wang, G.H. Cao, A.M. Russell, Z.J. Zhou, et al., Effect of heat treatment on microstructure evolution of Inconel 718 alloy fabricated by selective laser melting, J. Alloys. Compd. 764 (2018) 639–649, https://doi.org/10.1016/j.jallcom.2018.06.112.
[34] B. Xiao, R. Chen, J. Zhang, J. Zhang, Y. Zhou, J. Ju, et al., Additively manufactured heterogeneous precipitation-strengthened high-entropy alloys with high strength and ductility, Addit. Manuf. 77 (2023) 103795, https://doi.org/10.1016/j.addma.2023.103795.
[35] N. Kouraytem, J. Varga, B. Amin-Ahmadi, H. Mirmohammad, R.A. Chanut, A. D. Spear, et al., A recrystallization heat-treatment to reduce deformation anisotropy of additively manufactured Inconel 718, Mater. Des. 198 (2021) 109228, https://doi.org/10.1016/j.matdes.2020.109228.
[36] A. Keshavarzkermani, R. Esmaeilizadeh, P.D. Enrique, H. Asgari, N.Y. Zhou, A. Bonakdar, et al., Static recrystallization impact on grain structure and mechanical properties of heat-treated Hastelloy X produced via laser powder-bed fusion, Mater. Charact. 173 (2021) 110969, https://doi.org/10.1016/j.matchar.2021.110969.
[37] S. Gao, Z. Hu, M. Duchamp, P.S.R. Krishnan, S. Tekumalla, X. Song, et al., Recrystallization-based grain boundary engineering of 316L stainless steel produced via selective laser melting, Acta Mater. 200 (2020) 366–377, https://doi.org/10.1016/j.actamat.2020.09.015.
[38] X. Chen, J. Kong, S. Feng, K. Dong, Y. Liang, Q. Wang, et al., A precipitation-strengthened high-entropy alloy prepared by selective laser melting in-situ alloying and post-heat treatment, J. Alloys. Compd. 936 (2023) 168145, https://doi.org/10.1016/j.jallcom.2022.168145.
[39] D. Lin, L. Xu, H. Jing, Y. Han, L. Zhao, F. Minami, Effects of annealing on the structure and mechanical properties of FeCoCrNi high-entropy alloy fabricated via selective laser melting, Addit. Manuf. 32 (2020) 101058, https://doi.org/10.1016/j.addma.2020.101058.
[40] A. Turnali, S.A.H. Motaman, Y. Chang, B. Böttger, A. Serafeim, L. Sayk, et al., Evolution of microstructural heterogeneities in additively manufactured low-alloy steel, Addit. Manuf. 78 (2023) 103859, https://doi.org/10.1016/j.addma.2023.103859.
[41] V.K. Singh, D. Sahoo, M. Amirthalingam, S. Karagadde, SK. Mishra, Dissolution of the Laves phase and δ-precipitate formation mechanism in additively manufactured Inconel 718 during post printing heat treatments, Addit. Manuf. 81 (2024) 104021, https://doi.org/10.1016/j.addma.2024.104021.
[42] Y. Mu, L. He, S. Deng, Y. Jia, Y. Jia, G. Wang, et al., A high-entropy alloy with dislocation-precipitate skeleton for ultrastrength and ductility, Acta Mater. 232 (2022) 117975, https://doi.org/10.1016/j.actamat.2022.117975.
[43] J.H. Rao, Y. Zhang, K. Zhang, A. Huang, C.H. Davies, X. Wu, Multiple precipitation pathways in an Al-7Si-0.6Mg alloy fabricated by selective laser melting, Scr. Mater. 160 (2019) 66–69, https://doi.org/10.1016/j.scriptamat.2018.09.045.
[44] Y.T. Tang, C. Panwisawas, B.M. Jenkins, J. Liu, Z. Shen, E. Salvati, et al., Multi-length-scale study on the heat treatment response to supersaturated nickel-based superalloys: Precipitation reactions and incipient recrystallisation, Addit. Manuf. 62 (2023) 103389, https://doi.org/10.1016/j.addma.2023.103389.
[45] A.R. McAndrew, M. Alvarez Rosales, P.A. Colegrove, J.R. Hönnige, A. Ho, R. Fayolle, et al., Interpass rolling of Ti-6Al-4V wire + arc additively manufactured features for microstructural refinement, Addit. Manuf. 21 (2018) 340–349, https://doi.org/10.1016/j.addma.2018.03.006.
[46] D. Raabe, D. Ponge, M-M Wang, M. Herbig, M. Belde, H. Springer, 1 billion tons of nanostructure – segregation engineering enables confined transformation effects at lattice defects in steels, IOP Conf. Ser.: Mater. Sci. Eng. 219 (2017) 12006, https://doi.org/10.1088/1757-899X/219/1/012006.
[47] D. Raabe, S. Sandlöbes, J. Millán, D. Ponge, H. Assadi, M. Herbig, et al., Segregation engineering enables nanoscale martensite to austenite phase transformation at grain boundaries: A pathway to ductile martensite, Acta Mater. 61 (16) (2013) 6132–6152, https://doi.org/10.1016/j.actamat.2013.06.055.
[48] P. Köhnen, S. Ewald, J.H. Schleifenbaum, A. Belyakov, C. Haase, Controlling microstructure and mechanical properties of additively manufactured high-strength steels by tailored solidification, Addit. Manuf. 35 (2020) 101389, https://doi.org/10.1016/j.addma.2020.101389.
[49] S.A.H. Motaman, F. Kies, P. Köhnen, M. Létang, M. Lin, A. Molotnikov, et al., Optimal Design for Metal Additive Manufacturing: An Integrated Computational Materials Engineering (ICME) Approach, JOM 72 (3) (2020) 1092–1104, https://doi.org/10.1007/s11837-020-04028-4.
[50] P. Kumar, S. Huang, D.H. Cook, K. Chen, U. Ramamurty, X. Tan, et al., A strong fracture-resistant high-entropy alloy with nano-bridged honeycomb microstructure intrinsically toughened by 3D-printing, Nat. Commun. 15 (1) (2024) 841, https://doi.org/10.1038/s41467-024-45178-2.
[51] J. Ren, Y. Zhang, D. Zhao, Y. Chen, S. Guan, Y. Liu, et al., Strong yet ductile nanolamellar high-entropy alloys by additive manufacturing, Nature 608 (7921) (2022) 62–68, https://doi.org/10.1038/s41586-022-04914-8.
[52] P. Niu, R. Li, Z. Fan, P. Cao, D. Zheng, M. Wang, et al., Inhibiting cracking and improving strength for additive manufactured Al CoCrFeNi high entropy alloy via changing crystal structure from BCC-to-FCC, Addit. Manuf. 71 (2023) 103584, https://doi.org/10.1016/j.addma.2023.103584.
[53] Z. Sun, X. Tan, C. Wang, M. Descoins, D. Mangelinck, S.B. Tor, et al., Reducing hot tearing by grain boundary segregation engineering in additive manufacturing: example of an AlxCoCrFeNi high-entropy alloy, Acta Mater. 204 (2021) 116505, https://doi.org/10.1016/j.actamat.2020.116505.
[54] R. Feng, Y. Rao, C. Liu, X. Xie, D. Yu, Y. Chen, et al., Enhancing fatigue life by ductile-transformable multicomponent B2 precipitates in a high-entropy alloy, Nat. Commun. 12 (1) (2021) 3588, https://doi.org/10.1038/s41467-021-23689-6.
[55] Z. Liu, D. Zhao, P. Wang, M. Yan, C. Yang, Z. Chen, et al., Additive manufacturing of metals: Microstructure evolution and multistage control, J. Mater. Sci. Technol. 100 (2022) 224–236, https://doi.org/10.1016/j.jmst.2021.06.011.
[56] J.O Andersson, Thomas Helander, Lars Höglund, Pingfang Shi, Bo Sundman, Thermo-Calc & DICTRA, computational tools for materials science, CALPHAD. 26 (2) (2002) 273–312, https://doi.org/10.1016/S0364-5916(02)00037-8.
[57] B. Hallstedt, M. Noori, F. Kies, F. Oppermann, C. Haase, Thermodynamic database for multi-principal element alloys within the system Al–Co–Cr–Fe–Mn–Ni–C, CALPHAD. 83 (2023) 102644, https://doi.org/10.1016/j.calphad.2023.102644.
[58] C.A. Schneider, W.S. Rasband, KW. Eliceiri, NIH Image to ImageJ: 25 years of image analysis, Nat. Methods 9 (7) (2012) 671–675, https://doi.org/10.1038/nmeth.2089.
[59] G. Nolze, R. Hielscher, Orientations – perfectly colored, J. Appl. Crystallogr. 49 (5) (2016) 1786–1802, https://doi.org/10.1107/S1600576716012942.
[60] F. Bachmann, R. Hielscher, H. Schaeben, Grain detection from 2d and 3d EBSD data–specification of the MTEX algorithm, Ultramicroscopy. 111 (12) (2011) 1720–1733, https://doi.org/10.1016/j.ultramic.2011.08.002.
[61] F. Bachmann, R. Hielscher, H. Schaeben, Texture Analysis with MTEX – Free and Open Source Software Toolbox, SSP 160 (2010) 63–68, https://doi.org/10.4028/www.scientific.net/SSP.160.63.
[62] A. Hariharan, L. Lu, J. Risse, A. Kostka, B. Gault, E.A. Jägle, et al., Misorientation-dependent solute enrichment at interfaces and its contribution to defect formation mechanisms during laser additive manufacturing of superalloys, Phys. Rev. Materials 3 (12) (2019), https://doi.org/10.1103/PhysRevMaterials.3.123602.
[63] K. Thompson, D. Lawrence, D.J. Larson, J.D. Olson, T.F. Kelly, B. Gorman, In situ site-specific specimen preparation for atom probe tomography, Ultramicroscopy. 107 (2-3) (2007) 131–139, https://doi.org/10.1016/j.ultramic.2006.06.008.
[64] B.H. Toby, RB von Dreele, GSAS-II the genesis of a modern open-source all purpose crystallography software package, J. Appl. Crystallogr. 46 (2) (2013) 544–549, https://doi.org/10.1107/S0021889813003531.
[65] D. Field, L. Bradford, M. Nowell, T. Lillo, The role of annealing twins during recrystallization of Cu, Acta Mater. 55 (12) (2007) 4233–4241, https://doi.org/10.1016/j.actamat.2007.03.021.
[66] M-S Pham, B. Dovgyy, P.A. Hooper, C.M. Gourlay, A. Piglione, The role of side-branching in microstructure development in laser powder-bed fusion, Nat. Commun. 11 (1) (2020) 749, https://doi.org/10.1038/s41467-020-14453-3.
[67] The Materials Project. Materials Data on AlNi by Materials Project 2020. https://doi.org/10.17188/1190944.
[68] The Materials Project. Materials Data on FeCo by Materials Project 2020. https://doi.org/10.17188/1196095.
[69] M.R. Stoudt, E.A. Lass, D.S. Ng, M.E. Williams, F. Zhang, C.E. Campbell, et al., The Influence of Annealing Temperature and Time on the Formation of δ-Phase in Additively-Manufactured Inconel 625, Metall. Mater. Trans. a Phys. Metall. Mater. Sci. 49 (2018), https://doi.org/10.1007/s11661-018-4643-y.
[70] Marc Legros, Gerhard Dehm, Eduard Arzt, T.John Balk, Observation of Giant Diffusivity Along Dislocation Cores, Science (1979) 319 (5870) (2008) 1646–1649, https://doi.org/10.1126/science.1151771.
[71] H. Mehrer, Diffusion in solid metals and alloys, Springer-Verlag, 1990.
[72] T. Marlaud, A. Deschamps, F. Bley, W. Lefebvre, B. Baroux, Influence of alloy composition and heat treatment on precipitate composition in Al–Zn–Mg–Cu alloys, Acta Mater. 58 (1) (2010) 248–260, https://doi.org/10.1016/j.actamat.2009.09.003.
[73] J. Humphreys, G.S. Rohrer, A. Rollett, Recrystallization of Single-Phase Alloys. Recrystallization and Related Annealing Phenomena, Elsevier, 2017, pp. 245–304.
[74] D.A. Porter, K.E. Easterling, MY. Sherif, Phase transformations in metals and alloys, CRC Press, Boca Raton, FL, 2009.
[75] G. Gottstein, Physical Foundations of Materials Science, 1st ed., Springer, Berlin, Heidelberg, 2004.
[76] E.A. Anber, A.C. Lang, E.A. Lass, P.K. Suri, J.L. Hart, D.S. D'Antuono, et al., Insight into the kinetic stabilization of Al0.3CoCrFeNi high-entropy alloys, Materialia (Oxf) 14 (2020) 100872, https://doi.org/10.1016/j.mtla.2020.100872.
[77] J. Dąbrowa, W. Kucza, G. Cieślak, T. Kulik, M. Danielewski, J-W. Yeh, Interdiffusion in the FCC-structured Al-Co-Cr-Fe-Ni high entropy alloys: Experimental studies and numerical simulations, J. Alloys. Compd. 674 (2016) 455–462, https://doi.org/10.1016/j.jallcom.2016.03.046.
[78] B. Decreus, A. Deschamps, F de Geuser, P. Donnadieu, C. Sigli, M. Weyland, The influence of Cu/Li ratio on precipitation in Al–Cu–Li–x alloys, Acta Mater. 61 (6) (2013) 2207–2218, https://doi.org/10.1016/j.actamat.2012.12.041.
[79] J. Da Costa Teixeira, D.G. Cram, L. Bourgeois, T.J. Bastow, A.J. Hill, C. R. Hutchinson, On the strengthening response of aluminum alloys containing shear-resistant plate-shaped precipitates, Acta Mater. 56 (20) (2008) 6109–6122, https://doi.org/10.1016/j.actamat.2008.08.023.
[80] A. Deschamps, CR. Hutchinson, Precipitation kinetics in metallic alloys: Experiments and modeling, Acta Mater. 220 (2021) 117338, https://doi.org/10.1016/j.actamat.2021.117338.
[81] M.J. Anderson, J. Benson, J.W. Brooks, B. Saunders, HC. Basoalto, Predicting Precipitation Kinetics During the Annealing of Additive Manufactured Inconel

625 Components, Integr. Mater. Manuf. Innov. 8 (2) (2019) 154–166, https://doi.org/10.1007/s40192-019-00134-7.
[82] W. Chrominski, M. Lewandowska, Precipitation phenomena in ultrafine grained Al–Mg–Si alloy with heterogeneous microstructure, Acta Mater. 103 (2016) 547–557, https://doi.org/10.1016/j.actamat.2015.10.030.
[83] D. Scotto D'Antuono, J. Gaies, W. Golumbfskie, ML. Taheri, Direct measurement of the effect of cold rolling on β phase precipitation kinetics in 5xxx series aluminum alloys, Acta Mater. 123 (2017) 264–271, https://doi.org/10.1016/j.actamat.2016.10.060.
[84] A. Jagetia, M. Nartu, S. Dasari, A. Sharma, B. Gwalani, R. Banerjee, Ordering-mediated local nano-clustering results in unusually large Hall-Petch strengthening coefficients in high entropy alloys, Mater. Res. Lett. 9 (5) (2021) 213–222, https://doi.org/10.1080/21663831.2020.1871440.
[85] R.L Fleischer, Substitutional solution hardening, Acta Metallurgica 11 (3) (1963) 203–209, https://doi.org/10.1016/0001-6160(63)90213-X.
[86] J.Y. He, H. Wang, H.L. Huang, X.D. Xu, M.W. Chen, Y. Wu, et al., A precipitation-hardened high-entropy alloy with outstanding tensile properties, Acta Mater. 102 (2016) 187–196, https://doi.org/10.1016/j.actamat.2015.08.076.
[87] J.Y. He, W.H. Liu, H. Wang, Y. Wu, X.J. Liu, T.G. Nieh, et al., Effects of Al addition on structural evolution and tensile properties of the FeCoNiCrMn high-entropy alloy system, Acta Mater. 62 (2014) 105–113, https://doi.org/10.1016/j.actamat.2013.09.037.
[88] Z. Wu, H. Bei, G.M. Pharr, EP. George, Temperature dependence of the mechanical properties of equiatomic solid solution alloys with face-centered cubic crystal structures, Acta Mater. 81 (2014) 428–441, https://doi.org/10.1016/j.actamat.2014.08.026.
[89] S. Yoshida, T. Ikeuchi, T. Bhattacharjee, Y. Bai, A. Shibata, N. Tsuji, Effect of elemental combination on friction stress and Hall-Petch relationship in face-centered cubic high /medium entropy alloys, Acta Mater. 171 (2019) 201–215, https://doi.org/10.1016/j.actamat.2019.04.017.
[90] Z. Wu, Y. Gao, H. Bei, Thermal activation mechanisms and Labusch-type strengthening analysis for a family of high-entropy and equiatomic solid-solution alloys, Acta Mater. 120 (2016) 108–119, https://doi.org/10.1016/j.actamat.2016.08.047.
[91] S.A.H. Motaman, F. Roters, C. Haase, Anisotropic polycrystal plasticity due to microstructural heterogeneity: A multi-scale experimental and numerical study on additively manufactured metallic materials, Acta Mater. 185 (2020) 340–369, https://doi.org/10.1016/j.actamat.2019.12.003.
[92] H. Diao, D. Ma, R. Feng, T. Liu, C. Pu, C. Zhang, et al., Novel NiAl-strengthened high entropy alloys with balanced tensile strength and ductility, Materials Science and Engineering: A 742 (2019) 636–647, https://doi.org/10.1016/j.msea.2018.11.055.
[93] George Kim, Haoyan Diao, Chanho Lee, A.T. Samaei, Tu Phan, Maarten de Jong, et al., First-principles and machine learning predictions of elasticity in severely lattice-distorted high-entropy alloys with experimental validation, Acta Mater. 181 (2019) 124–138, https://doi.org/10.1016/j.actamat.2019.09.026.
[94] Y. Lu, J. Wang, S. Williams, L. Zhu, J. Ding, C. Diao, et al., Additive manufacturing of a functionally graded high entropy alloy using a hybrid powder-bed wire-based direct energy deposition approach, Addit. Manuf. 63 (2023) 103424, https://doi.org/10.1016/j.addma.2023.103424.
[95] T.G. Gallmeyer, S. Moorthy, B.B. Kappes, M.J. Mills, B. Amin-Ahmadi, AP. Stebner, Knowledge of process-structure-property relationships to engineer better heat treatments for laser powder bed fusion additive manufactured Inconel 718, Addit. Manuf. 31 (2020) 100977, https://doi.org/10.1016/j.addma.2019.100977.
[96] U.F. Kocks, H. Mecking, Physics and phenomenology of strain hardening: the FCC case, Prog. Mater. Sci. 48 (3) (2003) 171–273, https://doi.org/10.1016/S0079-6425(02)00003-8.
[97] H. Mughrabi, The α-factor in the Taylor flow-stress law in monotonic, cyclic and quasi-stationary deformations: Dependence on slip mode, dislocation arrangement and density, Current Opinion in Solid State and Materials Science 20 (6) (2016) 411–420, https://doi.org/10.1016/j.cossms.2016.07.001.
[98] M.R. Staker, DL. Holt, The dislocation cell size and dislocation density in copper deformed at temperatures between 25 and 700°C, Acta Metallurgica 20 (4) (1972) 569–579, https://doi.org/10.1016/0001-6160(72)90012-0.
[99] G.K. Williamson, RE. Smallman III, Dislocation densities in some annealed and cold-worked metals from measurements on the X-ray debye-scherrer spectrum, The Philosophical Magazine: A Journal of Theoretical Experimental and Applied Physics 1 (1) (1956) 34–46, https://doi.org/10.1080/14786435608238074.
[100] G. Williamson, W. Hall, X-ray line broadening from filed aluminium and wolfram, Acta Metallurgica 1 (1) (1953) 22–31, https://doi.org/10.1016/0001-6160(53)90006-6.
[101] Raymond Kwesi Nutor, Qingping Cao, Ran Wei, Qingmei Su, Gaohui Du, Xiaodong Wang, et al., A dual-phase alloy with ultrahigh strength-ductility synergy over a wide temperature range, Sci. Adv. 7 (34) (2021) eabi4404, https://doi.org/10.1126/sciadv.abi4404.
[102] S. Esmaeili, D.J. Lloyd, WJ. Poole, A yield strength model for the Al-Mg-Si-Cu alloy AA6111, Acta Mater. 51 (8) (2003) 2243–2257, https://doi.org/10.1016/S1359-6454(03)00028-4.
[103] J.F. Nie, B.C. Muddle, IJ. Polmear, The effect of precipitate shape and orientation on dispersion strengthening in high strength aluminium alloys, Materials Science Forum 217-222 (PART 2) (1996) 1257–1262, https://doi.org/10.4028/www.scientific.net/msf.217-222.1257.
[104] R.Y. Zhang, H.L. Qin, Z.N. Bi, J. Li, S. Paul, T.L. Lee, et al., Evolution of Lattice Spacing of Gamma Double Prime Precipitates During Aging of Polycrystalline Ni-Base Superalloys: An In Situ Investigation, Metall Mater Trans A 51 (2) (2020) 574–585, https://doi.org/10.1007/s11661-019-05536-y.
[105] H. Long, H. Wei, Y. Liu, S. Mao, J. Zhang, S. Xiang, et al., Effect of lattice misfit on the evolution of the dislocation structure in Ni-based single crystal superalloys during thermal exposure, Acta Mater. 120 (2016) 95–107, https://doi.org/10.1016/j.actamat.2016.08.035.
[106] L.M. Brown, GR. Woolhouse, The loss of coherency of precipitates and the generation of dislocations, The Philosophical Magazine: A Journal of Theoretical Experimental and Applied Physics 21 (170) (1970) 329–345, https://doi.org/10.1080/14786437008238420.
[107] W. Wu, P. Xia, H. Fu, W. Fan, N. Jiang, B. Gan, et al., Enhancing tensile properties by dual-precipitates in a CrFeNiVAl complex-concentrated alloy, Intermetallics. (Barking) 165 (2024) 108166, https://doi.org/10.1016/j.intermet.2023.108166.
[108] L. Li, J. Peng, S. Tang, Q. Fang, Y. Wei, Micromechanism of strength and damage trade-off in second-phase reinforced alloy by strain gradient plasticity theory, Int. J. Plast. 176 (2024) 103970, https://doi.org/10.1016/j.ijplas.2024.103970.
[109] D. Liu, Q. Yu, S. Kabra, M. Jiang, P. Forna-Kreutzer, R. Zhang, et al., Exceptional fracture toughness of CrCoNi-based medium- and high-entropy alloys at 20 kelvin, Science (1979) 378 (6623) (2022) 978–983, https://doi.org/10.1126/science.abp8070.
[110] C.E. Slone, J. Miao, E.P. George, MJ. Mills, Achieving ultra-high strength and ductility in equiatomic CrCoNi with partially recrystallized microstructures, Acta Mater. 165 (2019) 496–507, https://doi.org/10.1016/j.actamat.2018.12.015.
[111] C.E. Slone, V. Mazánová, P. Kumar, D.H. Cook, M. Heczko, Q. Yu, et al., Partially recrystallized microstructures expand the strength-toughness envelope of CrCoNi medium-entropy alloy, Commun. Mater. 5 (1) (2024), https://doi.org/10.1038/s43246-024-00704-z.
[112] G. Zhang, W. Ma, P. Ji, B. Zhang, X. Zhang, J. Zhang, et al., The effects of partial recrystallization annealing and aging treatment on the microstructural evolution and mechanical behavior of austenitic lightweight steel, Materials Science and Engineering: A 885 (2023) 145602, https://doi.org/10.1016/j.msea.2023.145602.
[113] J. Zhang, D. Raabe, CC. Tasan, Designing duplex, ultrafine-grained Fe-Mn-Al-C steels by tuning phase transformation and recrystallization kinetics, Acta Mater. 141 (2017) 374–387, https://doi.org/10.1016/j.actamat.2017.09.026.
[114] C. Haase, L.A. Barrales-Mora, F. Roters, D.A. Molodov, G. Gottstein, Applying the texture analysis for optimizing thermomechanical treatment of high manganese twinning-induced plasticity steel, Acta Mater. 80 (2014) 327–340, https://doi.org/10.1016/j.actamat.2014.07.068.